The global attenuation structure of the upper mantle

Colleen A. Dalton,[1,2] Göran Ekström,[2] and Adam M. Dziewoński[1]

Received 9 October 2007; revised 21 April 2008; accepted 19 June 2008; published 10 September 2008.

[1] A large data set of fundamental mode Rayleigh wave amplitudes is analyzed to derive a new global three-dimensional model of shear wave attenuation in the upper mantle. The amplitude observations span a range of periods between 50 and 250 s and are derived from earthquakes with $M_W > 6.0$ that occurred between 1993 and 2005. Four separate factors may influence an amplitude anomaly: intrinsic attenuation along the raypath, elastic focusing effects along the raypath, uncertainties in the strength of excitation, and uncertainties in the response at the station. In an earlier paper (Dalton and Ekström, 2006a), dependence of the retrieved attenuation structure on these terms was shown to be significant and an approach was developed to invert the amplitudes simultaneously for each term. The new three-dimensional attenuation model QRFSI12, which is the subject of this paper, is derived using this method. The model contains large lateral variations in upper-mantle attenuation, ±60% to ±100%, and exhibits strong agreement with surface tectonic features at depths shallower than 200 km. At greater depth, QRFSI12 is dominated by high attenuation in the southeastern Pacific and eastern Africa and low attenuation along many subduction zones in the western Pacific. Resolution tests confirm that the change in pattern of attenuation above and below 200-km depth can be determined with confidence using the fundamental mode data set. The new model is highly correlated with global models of shear wave velocity, particularly in the uppermost mantle, suggesting that the same factors may control both seismic attenuation and velocity in this depth range. However, forcing the lateral perturbations in attenuation to match those found in global velocity models decreases the data variance reduction, which suggests that subtle differences between patterns of attenuation and velocity are robust.

Citation: Dalton, C. A., G. Ekström, and A. M. Dziewoński (2008), The global attenuation structure of the upper mantle, *J. Geophys. Res.*, *113*, B09303, doi:10.1029/2007JB005429.

1. Introduction

[2] Observation of seismic wave attenuation provides a direct measure of the Earth's anelastic properties, and as such it is a potentially valuable source of information about the physical and chemical state of the interior of the planet. Historically, the majority of seismic imaging studies have mapped out variations in elastic wave speed [e.g., *Woodhouse and Dziewonski*, 1984; *Woodward and Masters*, 1991; *van der Hilst et al.*, 1997; *Ritsema et al.*, 1999; *Panning and Romanowicz*, 2006; *Kustowski et al.*, 2008], and there have been considerably fewer efforts to investigate attenuation in the Earth. However, the sensitivity of attenuation to factors such as temperature, composition, partial melt, and water content is different from that of seismic velocity [e.g., *Anderson*, 1967; *Hammond and Humphreys*, 2000a, 2000b; *Jackson et al.*, 2002, 2004; *Karato*, 2003; *Faul and Jackson*, 2005], and joint interpretation of elastic and anelastic models may be used to improve constraints on the relative importance of these competing effects in various regions of the Earth. Furthermore, attenuation leads to the physical dispersion of seismic velocities [*Liu et al.*, 1976]. It is necessary to account carefully for the effect of attenuation on velocity in order to infer temperature from velocity, especially in the upper mantle [*Karato*, 1993], to compare body wave, surface wave, and free oscillation data [*Kanamori and Anderson*, 1977], and to interpret seismic models together with the geoid [*Romanowicz*, 1990].

[3] The slow progress of attenuation model development (relative to models of wave speed) is not surprising since the wave amplitude, which is typically used to measure attenuation, requires a more complex interpretation than wave traveltime or phase delay. Uncertainty in the estimation of source excitation, focusing and scattering by elastic heterogeneity, and inaccuracies in the instrument response all complicate interpretation of a measured amplitude in terms of attenuation. Determining how to best account for these extraneous effects has been a primary objective of many attenuation studies. In a previous paper [*Dalton and Ekström*, 2006a], we described the various techniques that

[1]Department of Earth and Planetary Sciences, Harvard University, Cambridge, Massachusetts, USA.
[2]Lamont-Doherty Earth Observatory of Columbia University, Palisades, New York, USA.

0148-0227/08/2007JB005429$09.00

have been developed to isolate the signal of attenuation in surface-wave amplitude data. The approach we presented and advocated in that paper involves determining the extraneous terms as part of the inverse problem, and section 3 provides a review of this approach.

[4] There is reasonably good agreement regarding the gross features of the Earth's radial attenuation structure [e.g., *Sailor and Dziewonski*, 1978; *Dziewonski and Anderson*, 1981; *Anderson and Given*, 1982; *Durek and Ekström*, 1996; *Resovsky et al.*, 2005]. For example, dissipation in shear (Q_μ^{-1}) is considerably stronger than bulk attenuation (Q_κ^{-1}) in all layers. A zone of low Q_μ exists in a thin layer (~100–200 km thickness) in the shallow mantle, and the lower mantle is more weakly attenuating than the upper mantle. Attenuation in the inner core is characterized by Q_μ values around 100. It is worth noting that the majority of one-dimensional Q_μ^{-1} models were derived from low-frequency normal mode and surface-wave data; applicability to higher-frequency body waves depends on assumptions about the frequency dependence of attenuation [e.g., *Sipkin and Jordan*, 1979].

[5] Lateral variations in attenuation have been explored by a number of studies. Early analyses observed a qualitative relationship between tectonic province and magnitude of attenuation, using data sets such as the upper-mantle shear wave phase S_n [*Molnar and Oliver*, 1969], multiple *ScS* phases [*Sipkin and Jordan*, 1980], and mantle wave waveforms [*Dziewonski and Steim*, 1982]. Specifically, stable continental regions were found to be considerably less attenuating than areas of young oceanic crust and island arcs. These and later studies also documented a decrease of shallow mantle attenuation with increasing age of the ocean floor in the Pacific [*Canas and Mitchell*, 1978; *Sipkin and Jordan*, 1980; *Chan and Der*, 1988] and the Atlantic [*Canas and Mitchell*, 1981; *Sheehan and Solomon*, 1992] using diverse data sets that include fundamental mode surface waves and *SS-S* differential t* measurements in addition to the core-reflected phases.

[6] The existence of lateral attenuation variations within the subcontinental mantle has also been shown, with tectonically active regions causing greater seismic wave attenuation than stable regions, for example, in China [*Sipkin and Revenaugh*, 1994], Eurasia [*Chan and Der*, 1988], Australia [*Revenaugh and Jordan*, 1991], North America [*Lay and Wallace*, 1988; *Lawrence et al.*, 2006], and East Africa [*Venkataraman et al.*, 2004]. Regional studies near subduction zones have illuminated high shear attenuation within the mantle wedge above the subducting slab and less attenuation in the downgoing plate [e.g., *Flanagan and Wiens*, 1990; *Roth et al.*, 1999; *Stachnik et al.*, 2004]. In addition, high attenuation has been observed in the uppermost 150 km beneath the Lau back-arc spreading center [*Flanagan and Wiens*, 1990].

[7] Many of the observations listed above are qualitatively consistent with an important role for thermal variations in controlling the measured attenuation, notably greater-than-average attenuation for young oceanic lithosphere and actively deforming continental regions. More recently, studies have sought to understand the extent to which various features can and cannot be explained by temperature alone [e.g., *Roth et al.*, 2000; *Lawrence et al.*, 2006; *Yang et al.*, 2007]. Although not able to resolve structure on the same small scale as regional studies, global tomographic models are useful for characterizing large-scale relationships between various quantities, such as attenuation and temperature or attenuation and velocity, and also for detecting anomalous regions that deviate from the global trends. To date, six global three-dimensional models of upper-mantle attenuation have been published; the work presented here represents the seventh such effort. Three of these models were determined from surface-wave amplitude data [*Romanowicz*, 1995; *Selby and Woodhouse*, 2002; *Gung and Romanowicz*, 2004], and three were derived from body wave data [*Bhattacharyya et al.*, 1996; *Reid et al.*, 2001; *Warren and Shearer*, 2002]; no study has yet inverted both data sets together. In addition to those listed above, *Lawrence and Wysession* [2006] have developed a global lower-mantle attenuation model from body waves.

[8] The first global three-dimensional attenuation model [*Romanowicz*, 1995] was derived from measurements of fundamental mode Rayleigh wave amplitudes and imaged structure from the surface to 650-km depth with a horizontal resolution equivalent to spherical-harmonic degree 6. This model showed high attenuation beneath much of the Pacific and Atlantic ocean basins and low attenuation under almost all continental regions for depths <250 km. At greater depth, a correlation between high attenuation and the locations of hot spots was observed. *Bhattacharyya et al.* [1996] measured *SS-S* differential attenuation for ~3,000 globally recorded waveforms and attributed the observed values to upper-mantle structure beneath the *SS* bounce point. These data showed considerably lower attenuation for continental shields and platforms than for young oceanic regions. However, large-scale trends that relate attenuation to tectonic province were not readily apparent, which may reflect the limited spatial coverage and depth resolution of their data set. Alternatively, *Ritsema et al.* [2002] suggested that *SS-S* amplitude ratios contain significant signal due to focusing by velocity gradients in the mantle, which could affect interpretation of such data sets in terms of attenuation structure alone.

[9] *Reid et al.* [2001] used ~5,000 *SS-S* and *SSS-SS* differential measurements to constrain upper-mantle attenuation structure. The three-dimensional model that resulted from inversion of this data set was expanded in spherical harmonics up to degree 8 and exhibited high attenuation along much of the mid-ocean ridge system and at some convergent margins for depths shallower than 300 km. Low attenuation was generally associated with continental interiors, such as western Australia, northern North America, and much of Eurasia; highly attenuating South America was a notable exception to this trend. *Warren and Shearer* [2002] studied upper-mantle compressional attenuation with spectra from P and PP arrivals. Their data showed a clear, large-scale relationship between attenuative properties and tectonic regions; age-dependent behavior was apparent within the oceans, and continental shields and platforms exhibited considerably less attenuation than orogenic zones. The authors assumed all dissipative signal occurred in the upper 220 km and derived a three-dimensional model in which mid-ocean ridges were generally high-attenuation features and stable parts of Eurasia and North America were characterized by low attenuation.

[10] The model of *Selby and Woodhouse* [2002] was determined from a large data set of fundamental mode Rayleigh wave amplitudes. It was expanded in spherical harmonics up to degree 8 and extended from the surface to ~700-km depth, although constraints on features below 400 km were weak. Model QRLW8 [*Gung and Romanowicz*, 2004] was derived from three-component surface-wave waveform data in the period range 60–400 s. This spherical-harmonic degree-8 model extended to 660-km depth, and the inclusion of overtones in the waveform data set allowed better constraints on structure in the transition zone than was true for earlier surface-wave studies. Both QRLW8 and the model of *Selby and Woodhouse* [2002] exhibited low attenuation beneath many continental interiors and generally high attenuation under the oceans in the shallow mantle. Furthermore, at depths greater than 300 km, QRLW8 contained high-attenuation anomalies under the southern Pacific and Africa that were correlated with hot spot distribution. We have previously pointed out [*Dalton and Ekström*, 2006a] that certain features in both models, such as low attenuation along the southern East Pacific Rise and western North America at ~100-km depth, may be biased by failure to remove focusing effects from the amplitude data.

[11] In this study, we determine a new global three-dimensional model of shear attenuation in the upper mantle. The construction of this new model differs from earlier efforts in both the quantity and the interpretation of the surface-wave amplitude data. We use more than 30,000 amplitude measurements at each frequency, and we follow the approach described by *Dalton and Ekström* [2006a], hereinafter referred to as DE06a, to invert the amplitudes simultaneously for the coefficients of the three-dimensional attenuation model as well as for frequency-dependent correction factors for each source and receiver. Focusing and defocusing by elastic heterogeneity have been shown to influence significantly surface-wave amplitudes [e.g., *Woodhouse and Wong*, 1986; *Selby and Woodhouse*, 2000; *Dalton and Ekström*, 2006a, 2006b]; here focusing effects are removed from the data prior to inversion, an approach that greatly simplifies the inverse problem and has negligible consequences for the retrieved attenuation structure.

[12] Our new model contains strong regional trends in attenuation for depths <200 km, with a clear dependence on seafloor age within oceanic regions and a relationship to tectonic province in continental areas. Agreement with earlier attenuation studies is variable and generally weak, with correlation coefficients <0.5 throughout the upper mantle. The attenuation model also exhibits a stronger correlation with global models of shear wave velocity than any previous attenuation model does. In sections 2 and 3, the data set of amplitudes and the inversion procedure are described. The new three-dimensional attenuation model, hereinafter referred to as QRFSI12, is presented in section 4 along with the results of numerous tests to evaluate the sensitivity and robustness of the model. In section 5, QRFSI12 is compared with global shear wave velocity and attenuation models. The name of our preferred model, QRFSI12, is chosen to reflect that this attenuation model (Q) is derived from Rayleigh wave amplitudes (R), that focusing (F), source (S), and instrument (I) effects on the data have been accounted for, and that the model is expanded in spherical harmonics up to and including degree 12.

2. Data

[13] Seismic surface waves provide the strongest constraints on global upper-mantle structure. Phase anomalies constrain the average velocity anomaly along the raypath, arrival angles are primarily sensitive to the first transverse derivative of phase velocity, and amplitudes depend on both attenuation structure as well as the second transverse derivative of velocity. Phase anomalies are by far the most widely used of these three data sets [e.g., *Trampert and Woodhouse*, 1995; *Laske and Masters*, 1996; *Ekström et al.*, 1997], whereas the other two have so far had only limited application.

[14] The attenuation model described in this paper is derived from observations of fundamental mode Rayleigh wave amplitude anomaly in the period range 50–250 s. The data are measured from vertical-component seismograms derived from earthquakes with $M_W > 6.0$ that were recorded by the stations of the Global Seismographic Network (GSN) of the Incorporated Research Institutions for Seismology (IRIS) operated by the USGS and the University of California at San Diego, the China Digital Seismograph Network (CDSN), the Global Telemetered Seismograph Network (GTSN), and the MEDNET and GEOSCOPE networks. The algorithm described by *Ekström et al.* [1997] is used to make the measurements. The data are ratios of observed to synthetic wave amplitude, where the reference seismogram is calculated using the appropriate moment tensor and centroid location from the Harvard CMT catalog [*Dziewonski et al.*, 1981], the reported instrument response, and one-dimensional Earth structure from PREM [*Dziewonski and Anderson*, 1981]. We have also analyzed fundamental mode Love wave amplitudes but do not include those data owing to generally weaker signal-to-noise levels on the horizontal components.

[15] For the development of QRFSI12, the data set used by DE06a has been expanded to include earthquakes that occurred between 2003 and 2005, extending the original time period 1993–2002 by 3 years. The inclusion of the new data increases the total number of amplitude measurements by 88,000–111,000 at each period. The primary benefit afforded by the larger data set is the use of more restrictive quality criteria for the selection of amplitudes to be used in the inversion for three-dimensional attenuation structure. The amplitudes are selected based on (1) the level of fit between the observed and reference seismograms, (2) requirement of at least 20° of epicentral distance between a receiver and the source or its antipode, and (3) the number of paths associated with each earthquake and receiver. For periods shorter than 150 s, each earthquake and receiver is required to have at least 50 and 70 observations associated with it, respectively. For periods between 150 and 200 s, each earthquake and receiver must have at least 60 observations. At longer periods, this requirement is increased to 100 observations. For periods ≥150 s, multiple Rayleigh wave orbits are included; thus the requirement of 100 observations can include multiple

Table 1. Summary of Amplitude Data Used for the Three-Dimensional Attenuation Model[a]

Period, s	Total no. of amplitudes: 1993–2005	No. of amplitudes used	No. of events	No. of stations	No. of R1	No. of R2	No. of R3	No. of R4
50	343,186	33,863	513	193	33,863	0	0	0
75	343,231	34,089	514	193	34,089	0	0	0
100	343,186	34,447	519	195	34,447	0	0	0
125	343,186	34,530	521	195	34,530	0	0	0
150	215,775	32,330	261	196	15,560	16,770	0	0
175	215,775	32,308	260	196	15,562	16,746	0	0
200	215,775	32,405	261	195	15,668	16,737	0	0
225	215,775	50,152	256	192	20,560	17,708	9426	2458
250	215,775	50,304	257	192	20,656	17,745	9441	2462

[a]Column 2 reports the total number of amplitude observations made for earthquakes that occurred between 1993 and 2005, and column 3 indicates the total number used in the inversion, once the selection criteria described in the text have been applied.

orbits for the same station or earthquake. The final data set is summarized in Table 1.

3. Method

[16] The attenuation of a fundamental mode surface wave with frequency ω, $Q^{-1}(\omega)$, is related to the Earth's intrinsic bulk attenuation, $Q_\kappa^{-1}(r)$, and shear attenuation, $Q_\mu^{-1}(r)$, by

$$Q^{-1}(\omega) = \int_0^a \left[\kappa_0(r)K_\kappa(\omega,r)Q_\kappa^{-1}(r) + \mu_0(r)K_\mu(\omega,r)Q_\mu^{-1}(r)\right]r^2dr, \tag{1}$$

where integration over the radius r proceeds from the center of the Earth to the surface ($r = a$). The quantities κ_0K_κ and μ_0K_μ (Figure 1) are the compressional and shear energy densities (more commonly known as sensitivity kernels), respectively [*Backus and Gilbert*, 1967]. If Q^{-1}, Q_κ^{-1}, and Q_μ^{-1} are allowed to vary laterally, then

$$Q^{-1}(\omega,\theta,\phi) = \int_0^a \left[\kappa_0(r)K_\kappa(\omega,r)Q_\kappa^{-1}(r,\theta,\phi) + \mu_0(r)K_\mu(\omega,r)Q_\mu^{-1}(r,\theta,\phi)\right]r^2dr. \tag{2}$$

[17] To relate a measured amplitude anomaly, $A(\omega)$, to the Earth's intrinsic attenuation structure, we recall the approach outlined by DE06a,

$$A(\omega) = A^S(\omega)A^I(\omega)A^F(\omega)A^Q(\omega), \tag{3}$$

where A^S is due to excitation at the source, A^I accounts for receiver-related effects on amplitude, A^F is the geometrical spreading factor, and A^Q describes the decay due to attenuation along the raypath. Since the amplitude observa-

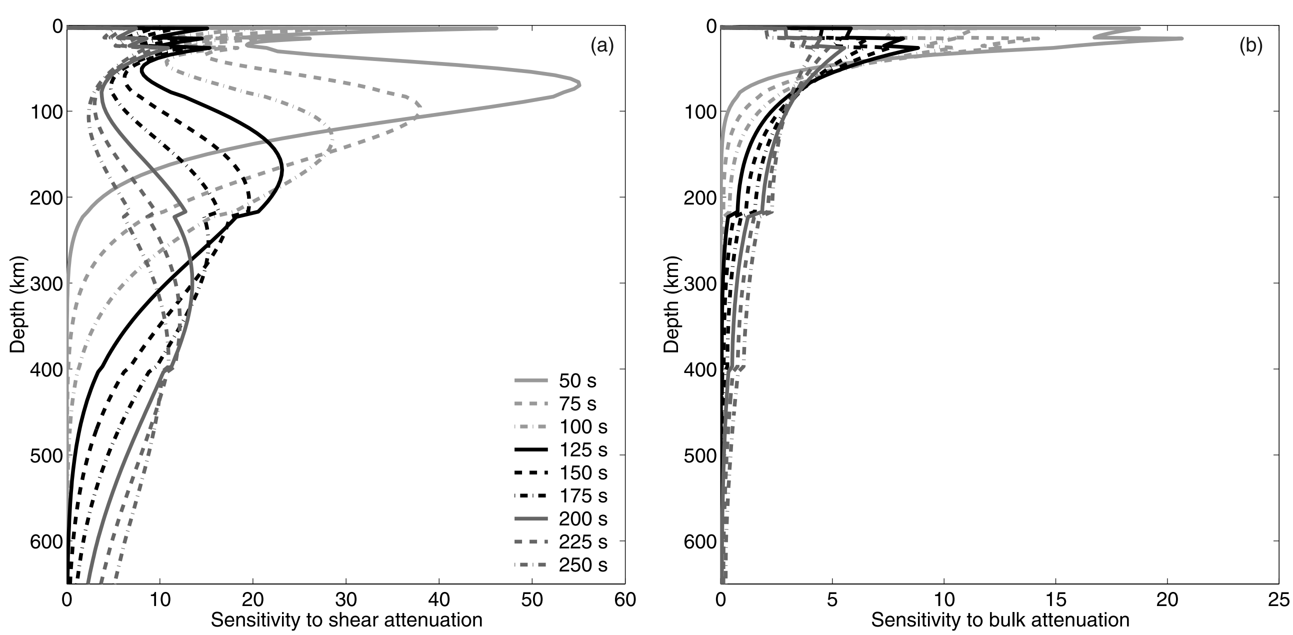

Figure 1. Rayleigh wave sensitivity kernels for the nine frequencies including in this study, calculated for PREM. (a) Sensitivity of the fundamental mode waves to shear attenuation. (b) Sensitivity of the fundamental mode waves to bulk attenuation. Note the different horizontal scales.

tions are made with respect to a reference seismogram, values of A^{S}, A^{I}, A^{F}, and A^{Q} not equal to unity represent deviations away from the assumed source, receiver, geometrical spreading, and attenuation parameters. The effect of attenuation on the surface-wave amplitude anomaly is given by

$$A^{\mathrm{Q}}(\omega) = \exp\left[-\frac{\omega}{2U(\omega)}\int_S^R \delta Q^{-1}(\omega,\theta,\phi)ds\right], \quad (4)$$

where the attenuation anomaly, $\delta Q^{-1}(\omega, \theta, \phi)$, is integrated along the raypath connecting the source S and receiver R, and $U(\omega)$ is the group velocity. For an amplitude observation corresponding to the ith earthquake and the jth receiver, equation (4) can be written

$$A_{ij}^{\mathrm{Q}}(\omega) = \exp\left[-\frac{\omega X_{ij}}{2U(\omega)}\overline{\delta Q_{ij}^{-1}}(\omega)\right], \quad (5)$$

where X_{ij} is the length of the path and $\overline{\delta Q_{ij}^{-1}}(\omega)$, the path-averaged attenuation anomaly, is with respect to the attenuation predicted by PREM [*Dziewonski and Anderson*, 1981],

$$\overline{\delta Q_{ij}^{-1}}(\omega) = \frac{1}{X_{ij}}\int_{S_i}^{R_j} Q^{-1}(\omega,\theta,\phi)ds - Q_{PREM}^{-1}(\omega). \quad (6)$$

[18] Combining equations (3), (5), and (6) leads to

$$\frac{-2U}{\omega X_{ij}}\ln A_{ij} + Q_{PREM}^{-1} = \frac{-2U}{\omega X_{ij}}\left[\ln A_i^{\mathrm{S}} + \ln A_j^{\mathrm{I}} + \ln A_{ij}^{\mathrm{F}}\right] + \frac{1}{X_{ij}}\int_{S_i}^{R_j} Q^{-1}(\theta,\phi)ds, \quad (7)$$

and it is understood that equation (7) applies at a specific frequency ω.

[19] Throughout the mantle, $Q_\kappa \gg Q_\mu$ [e.g., *Durek and Ekström*, 1996], and furthermore, the fundamental mode Rayleigh waves utilized in this study have minimal sensitivity to attenuation in bulk (Figure 1). By attributing all of the observed surface-wave dissipation to shear attenuation, an observed amplitude anomaly can be related to three-dimensional shear attenuation by

$$\frac{-2U}{\omega X_{ij}}\ln A_{ij} + Q_{PREM}^{-1} = \frac{-2U}{\omega X_{ij}}\left[\ln A_i^{\mathrm{S}} + \ln A_j^{\mathrm{I}} + \ln A_{ij}^{\mathrm{F}}\right] + \frac{1}{X_{ij}}\int_{S_i}^{R_j}\int_0^a \mu_0(r)K_\mu(\omega,r)Q_\mu^{-1}(r,\theta,\phi)r^2 drds. \quad (8)$$

[20] There are three important modifications to equation (8). One, we do not want to solve for crustal attenuation from the amplitude data, as the intermediate- and long-period fundamental mode Rayleigh waves used here are not sufficiently sensitive to anelastic structure at crustal depths (Figure 1). In the determination of our preferred attenuation model, described in section 4, we assume a constant crustal thickness of 24.4 km and a crustal Q_μ value of 600 [*Dziewonski and Anderson*, 1981]. As detailed in section 4.1, we have experimented with a range of crustal Q_μ values as well as laterally variable crustal thickness and concluded that the influence of assumptions about crustal attenuation on the retrieved mantle attenuation model is minimal.

[21] Two, because it is necessary to regularize the inverse problem, it is desirable to solve for perturbations $\delta Q_\mu^{-1}(r, \theta, \phi)$ with respect to a reference attenuation model, Q_{ref}^{-1}. For the determination of our preferred model, Q_{ref}^{-1} depends only on radius, although as discussed in section 5.3, we have also investigated the implications of using a three-dimensional reference model. In all cases, the sensitivity functions $\mu_0(r)$ $K_\mu(\omega, r)$ are calculated in PREM.

[22] Three, rather than solving for them, we remove focusing effects from each amplitude datum prior to inversion. Amplitudes are focused and defocused by lateral velocity heterogeneity, and in two earlier studies [DE06a; *Dalton and Ekström*, 2006b] we demonstrated that amplitudes can provide valuable constraints on phase-velocity maps, particularly when phase-delay measurements are included as additional constraint. In deriving two-dimensional Rayleigh wave attenuation maps (DE06a), we accounted for the effect of focusing on amplitudes by solving for phase-velocity maps as part of the inverse problem. However, this approach would require significant computational expense for the three-dimensional problem described here, increasing the total number of unknown parameters from 6461 to 10,430 and nearly tripling the number of computational steps. Instead, we use the phase-velocity maps determined from simultaneous inversion of phase and amplitude data described by DE06a to remove focusing effects a priori, and we have determined that doing so has no detectable effect on the retrieved attenuation structure. The ray theoretical expressions of *Woodhouse and Wong* [1986] are used to predict amplitude anomalies from phase-velocity variations. Hereinafter, the variable A_{ij}^{CF} will be used to indicate measurements of surface-wave amplitude that have been corrected for focusing effects, i.e., $A_{ij}^{\mathrm{CF}} = A_{ij}/A_{ij}^{\mathrm{F}}$.

[23] To justify this approach, we performed a test that compared two sets of two-dimensional Rayleigh wave attenuation maps. The first set of maps was determined using the method described by DE06a: surface-wave amplitude and phase-delay data were simultaneously inverted for two-dimensional attenuation maps, two-dimensional phase-velocity maps, and source and receiver factors. For the second set of maps, the amplitude data were first corrected for focusing effects using the phase-velocity maps determined from the simultaneous inversion of amplitude and phase data. These corrected data were then inverted for two-dimensional attenuation maps, and source and receiver factors. Correlation coefficients for the two sets of maps are very high, >0.99 at all periods, indicating that the retrieved attenuation structure does not depend on whether focusing effects are accounted for during or prior to the inversion. It is, however, important that the assumed elastic structure is consistent with the amplitude data, which are sensitive to short-wavelength velocity variations. We have previously shown that phase-velocity maps determined from both amplitude and phase-delay data have less power at high spherical-harmonic degrees than maps determined from phase measurements only (DE06a).

[24] The three-dimensional perturbations in attenuation, $\delta Q_\mu^{-1}(r, \theta, \phi)$, are parameterized horizontally in terms of spherical harmonics and radially in terms of one-dimensional cubic B-splines

$$\delta Q_\mu^{-1}(r,\theta,\phi) = \sum_{k=1}^{K}\sum_{l=0}^{L}\sum_{m=-l}^{l} q_{klm} B_k(r) Y_{lm}(\theta,\phi), \tag{9}$$

where q_{klm} are the coefficients that multiply the basis functions, and the sum is over the K radial splines $B_k(r)$ and the degree l and order m of the spherical-harmonic function $Y_{lm}(\theta, \phi)$ with maximum degree L.

[25] With these considerations, equation (8) becomes

$$\begin{aligned}
&\frac{-2U}{\omega X_{ij}} \ln A_{ij}^{\mathrm{CF}} + Q_{PREM}^{-1} \\
&\quad - \frac{1}{X_{ij}} \int_{S_i}^{R_j} \int_{r_c}^{a} \mu_0(r) K_\mu(\omega, r) Q_\mu^{-1}(r,\theta,\phi) r^2 dr ds \\
&\quad - \frac{1}{X_{ij}} \int_{S_i}^{R_j} \int_{0}^{r_c} \mu_0(r) K_\mu(\omega, r) Q_{\mathrm{ref}}^{-1}(r) r^2 dr ds \\
&= \frac{-2U}{\omega X_{ij}} \left[\ln A_i^{\mathrm{S}} + \ln A_j^{\mathrm{I}}\right] + \sum_k \sum_l \sum_m q_{klm} \overline{Y_{lm}} Z_k(\omega),
\end{aligned} \tag{10}$$

where r_c indicates the radius of the Moho, $\overline{Y_{lm}}$ is the path average of the spherical-harmonic function, and

$$Z_k(\omega) = \int_0^{r_c} \mu_0(r) K_\mu(\omega, r) B_k(r) dr. \tag{11}$$

[26] Equation (10) summarizes the inverse problem: given a set of amplitude observations A_{ij}^{CF}, what are the coefficients of the attenuation model q_{klm} and the frequency-dependent source and receiver factors $A^{\mathrm{S}}{}_i(\omega)$ and $A^{\mathrm{I}}{}_j(\omega)$ that best explain the data? In matrix notation, the inverse problem can be written

$$\mathsf{G} \cdot \mathsf{x} = \mathsf{d} + \mathsf{e}, \tag{12}$$

where the vector d contains the data (with corrections for crustal attenuation and reference model) to be fit, i.e.,

$$\begin{aligned}
\mathsf{d} = &\frac{-2U}{\omega X_{ij}} \ln A_{ij}^{\mathrm{CF}} + Q_{PREM}^{-1} \\
&- \frac{1}{X_{ij}} \int_{S_i}^{R_j} \int_{r_c}^{a} \mu_0(r) \cdot K_\mu(\omega, r) Q_\mu^{-1}(r,\theta,\phi) r^2 dr ds \\
&- \frac{1}{X_{ij}} \int_{S_i}^{R_j} \int_{0}^{r_c} \mu_0(r) K_\mu(\omega, r) Q_{\mathrm{ref}}^{-1}(r) r^2 dr ds,
\end{aligned} \tag{13}$$

and the vector x contains the estimates of the coefficients to be determined, q_{klm}, A_i^{S}, and A_j^{I}. The sensitivity matrix G relates these two quantities and is assumed to be known from the forward problem. We seek a solution x to equation (12) such that a chosen measure of error, E, is minimized. Using a least squares approach, $E = \mathsf{e}^{\mathsf{T}}\mathsf{e} = |\mathsf{G} \cdot \mathsf{x}_{\mathsf{LS}} - \mathsf{d}|^2$ is minimized, where x_{LS} is the least squares solution to the inverse problem.

[27] Because the amplitude measurements used in this study are imperfect, are in some cases inconsistent with each other, and provide uneven raypath coverage, the solution of the inverse problem requires the addition of a priori constraints. We choose to minimize a measure of the model roughness, $\mathcal{R}$, defined here as the squared gradient of the attenuation perturbation:

$$\begin{aligned}
\mathcal{R} &= \int_V |\nabla \delta Q_\mu^{-1}(r,\theta,\phi)|^2 dV \\
&= \int_V \left[\left(\nabla \delta Q_\mu^{-1}(r,\theta,\phi)\right) \cdot \left(\nabla \delta Q_\mu^{-1}(r,\theta,\phi)\right)\right] dV.
\end{aligned} \tag{14}$$

[28] Equation (14) can be implemented as a linear constraint, $\mathsf{B} \cdot \mathsf{x} = \mathsf{c}$, and equation (12) becomes

$$\begin{bmatrix} \mathsf{G} \\ \lambda \mathsf{B} \end{bmatrix} \cdot \mathsf{x} = \begin{bmatrix} \mathsf{d} \\ \lambda \mathsf{c} \end{bmatrix} + \mathsf{e}, \tag{15}$$

where the parameter λ controls the relative weight of the damping constraint. In practice, we prefer to damp the radial and horizontal components of the model gradients separately; the damping factors that control vertical and horizontal smoothness are indicated using λ_{V} and λ_{H}, respectively. We note that equations (14) and (15) can be simplified by making use of the relation $\nabla_1^2 Y_{lm} = l(l + 1)$, where l is the spherical-harmonic degree and ∇_1 is the surface gradient [*Dahlen and Tromp*, 1998]. Given the relatively small size of the inverse problem addressed here, the exact least squares solution can be found using Cholesky factorization.

4. Attenuation Model

[29] Model QRFSI12 is constructed by applying equation (10) to the amplitude data set described in section 2. Horizontally, the perturbations in attenuation are expanded with spherical harmonics to degree 12, which provides a resolving half-wavelength of ~1700 km. Vertically, eight radial spline functions (Figure 2) are distributed from 24.4 km to 650 km, with narrower spacing in the shallow upper mantle to take advantage of the greater sensitivity of the fundamental mode surface waves in that region. The number of unknown model coefficients is $8 \times (12 + 1)^2 = 1352$, the number of unknown source factors is 3362 (Table 1), and the number of unknown receiver factors is 1747 for a grand total of 6461 unknown values to be determined.

[30] Depth slices of QRFSI12 are shown in Figure 3. The color scale shows the deviation in Q_μ^{-1} away from the globally averaged value. We prefer to report lateral attenuation variations with this convention rather than as a fractional perturbation in attenuation, $\frac{\delta Q_\mu^{-1}}{Q_\mu^{-1}}$, so that changes in the amplitude of anomalies with depth are apparent. In addition to the model coefficients, frequency-dependent source and receiver correction factors are also determined from the inversion (equation (10)). These values are extremely similar to those determined simultaneously with the two-dimensional Rayleigh wave attenuation maps discussed by DE06a; correlation coefficients between the two sets of values are greater than 0.993 at all periods. In DE06a, we demonstrated that many of the source factors with values $\neq 1$ are consistent with uncertainty in the earthquake depth and, by association, uncertainty in the estimated scalar

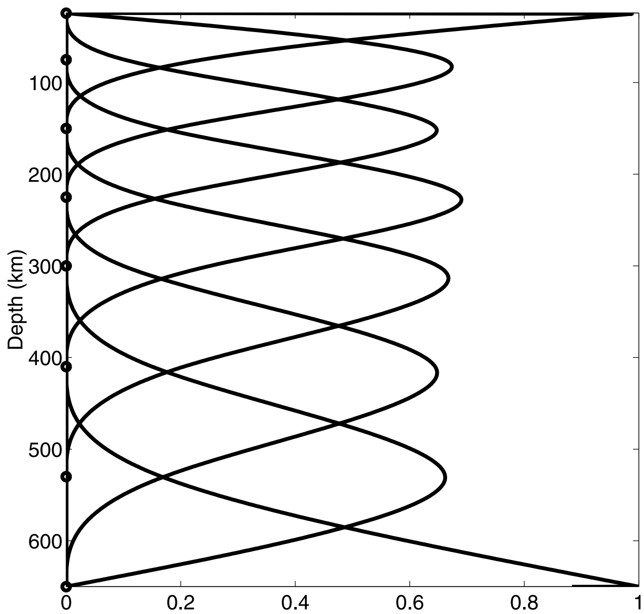

Figure 2. Distribution of radial splines used as the vertical basis functions for the three-dimensional attenuation model. Black circles along the vertical axis indicate the depth of each spline knot.

moment. The receiver factors were shown to strongly correlate with observations of instrument gain corrections that were independently determined [*Ekström et al.*, 2006]. Since these results remain essentially unchanged, we do not discuss the source and receiver factors further in this paper.

[31] The patterns of attenuation in Figure 3 can be divided, to first order, into two groups: attenuation above 250 km, and attenuation below 250 km. Resolution tests (section 4.3) demonstrate that our data set can robustly resolve distinct patterns in these two depth ranges. A change in pattern was also observed by *Gung and Romanowicz* [2004] in their attenuation model, QRLW8. Above 250 km, attenuation agrees well with surface-tectonic features, particularly at 100 km. Mid-ocean ridges are characterized by higher-than-average attenuation; this is true for the East Pacific Rise, the Pacific–Antarctic ridge, the Indian–Antarctic ridge, the Mid-Indian ridge, and the Mid-Atlantic ridge. High attenuation is also seen in the Lau Basin back-arc spreading center, along western North America, and in the central Pacific. The majority of regions characterized by lower-than-average attenuation are stable continental interiors, such as the Canadian Shield, the Amazonian craton, the cratons of Africa, the Russian platform, the Indian Shield, and the Yilgarn and Pilbara cratons of western Australia.

[32] The patterns are largely the same at 200 km, although the mid-ocean ridges are considerably weaker than at 100 km, and some are not characterized by high attenuation at this depth. We cannot rule out the possibility that the high attenuation along ridges at 200 km is the result of smearing from shallower depths. Below 250 km, the pattern changes, and the high-attenuation regions are concentrated in the southeastern Pacific and beneath eastern Africa. Low attenuation is associated with several of the subduction zones in the western Pacific and also beneath northern Eurasia.

[33] The primary features of the attenuation model are robust and well constrained; however, the amplitude of the variations in attenuation depends on the amount of damping applied to the inversion. Stronger damping results in a smoother model with weaker lateral variations. The sensitivity of the model to damping is discussed further in section 4.2.

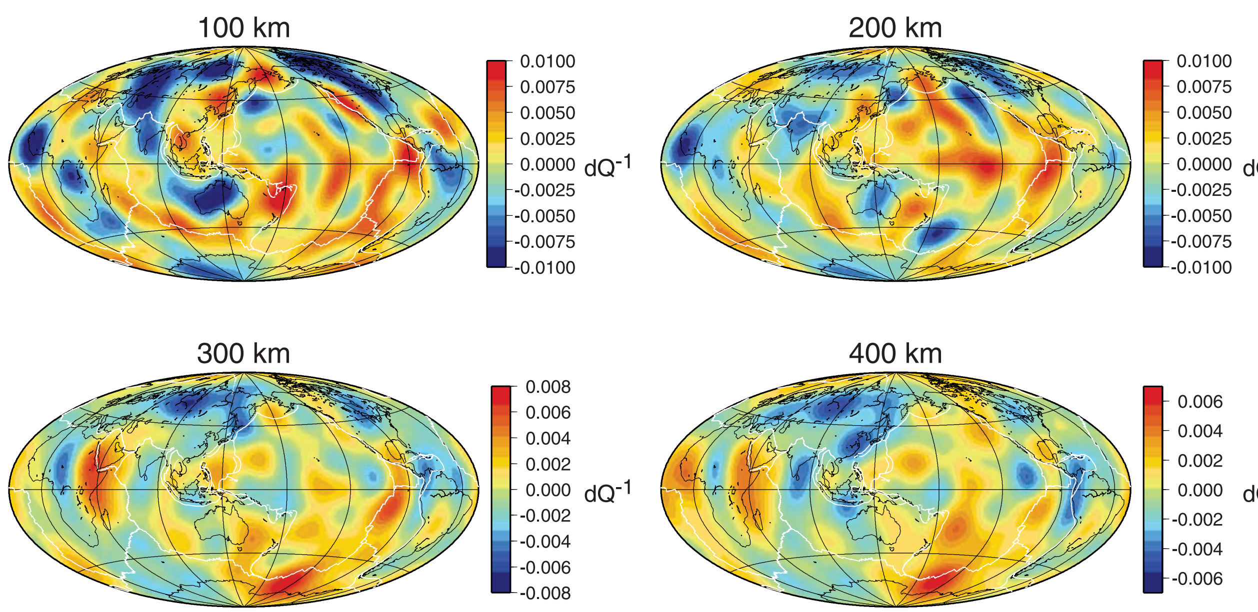

Figure 3. The three-dimensional shear attenuation model QRFSI12 plotted as the deviation away from the globally averaged Q_{μ}^{-1} at each depth. Expressed in terms of fractional perturbations to the average global value, the variations correspond to −100–80%, −73–70%, −79–91%, and −97–113% at 100-, 200-, 300-, and 400-km depth, respectively.

Table 2. Variance Reduction (%) for the Surface-Wave Amplitude Data Sets[a]

Period, s	Three-Dimensional Attenuation Model	Two-Dimensional Attenuation Maps	A^S and A^I Values Only	Degree-0 and A^S and A^I
50	47.0	47.2	20.5	30.5
75	46.2	46.5	23.8	30.7
100	46.4	46.8	30.1	35.0
125	51.4	52.0	41.5	43.9
150	32.4	34.4	18.8	24.1
175	32.8	33.8	25.7	26.6
200	40.9	42.0	35.2	35.2
225	33.5	34.5	30.3	31.0
250	38.7	39.5	35.6	36.9

[a]For both the three-dimensional attenuation model and the two-dimensional attenuation maps, the calculation of variance reduction includes the source and receiver factors that are simultaneously determined. The two-dimensional maps used for this calculation were not regularized and, as such, represent a maximum value variance reduction. Also listed here is the variance reduction calculated using only the source and receiver factors determined from the three-dimensional inversion and that calculated using the degree-zero component of the three-dimensional attenuation model together with the source and receiver factors.

[34] The residual variance reduction obtained for the data at each period is summarized in Table 2. Variance reduction is calculated as

$$\text{variance reduction} = 100 \times \left[1 - \frac{\sum_{n=1}^{N} \left(d_n^{\text{obs}} - d_n^{\text{pred}} \right)^2}{\sum_{n=1}^{N} \left(d_n^{\text{obs}} \right)^2} \right], \quad (16)$$

where, for the nth path,

$$d_n^{\text{obs}} = \frac{-2U}{\omega X_n} \ln A_n^{\text{CF}} \quad (17)$$

and

$$\begin{aligned} d_n^{\text{pred}} = & \sum_k \sum_l \sum_m q_{klm} \overline{Y_{lm}} Z_k(\omega) + \frac{-2U}{\omega X_n} \left[\ln A_n^{\text{S}} + \ln A_n^{\text{I}} \right] - Q_{PREM}^{-1} \\ & + \frac{1}{X_n} \int_{S_n}^{R_n} \int_{r_c}^{a} \mu_0(r) K_\mu(\omega, r) Q_\mu^{-1}(r, \theta, \phi) r^2 dr ds \\ & + \frac{1}{X_n} \int_{S_n}^{R_n} \int_{0}^{r_c} \mu_0(r) K_\mu(\omega, r) Q_{\text{ref}}^{-1}(r) r^2 dr ds. \end{aligned} \quad (18)$$

[35] In these equations, N is the total number of amplitude observations, and A_n^{S} and A_n^{I} are the source and receiver factors corresponding to the nth observation. In equation (18), the terms related to the reference model and the crust are included together with the model coefficients determined from the inversion. Formulating the variance reduction calculation in this way facilitates a comparison between models obtained with different reference models or different assumptions about the crust. For a three-dimensional model that fits the data well, the variance reduction should be similar to that obtained by the two-dimensional attenuation maps of DE06a. For comparison with the three-dimensional model, the two-dimensional maps described in DE06a were recalculated using the updated amplitude data set that contains earthquakes from 1993–2005, as the analysis in DE06a included only data through 2002. The calculation of variance for both the two-dimensional maps and the three-dimensional model includes the source and receiver factors that are simultaneously determined. The variance reduction obtained by the source and receiver factors only is provided in Table 2; the difference between the column 2 and column 4 in Table 2 is the improvement in data fit provided by the attenuation model. At all periods, the three-dimensional attenuation model improves the variance reduction over the source and receiver factors only by as much as 26% at 50 s and 3–5% at the longest periods. Using only the spherically symmetric part of the attenuation model, together with the source and receiver factors, improves the data fit by 0–10% over using source and receiver factors only; the difference between column 2 and column 5 in Table 2 is the improvement in data fit provided by the lateral attenuation variations.

[36] Figure 4 shows the globally averaged attenuation profiles obtained from the inversion. The detailed shape of the average global profile depends on the reference profile assumed; for this reason, results corresponding to two different reference models are shown in Figure 4. Reference model 1, a smooth version of the shear attenuation in PREM, contains sharp gradients above and below the low-Q_μ zone between 80 and 200 km, and reference model 2 is constant at $Q_\mu = 146$ throughout the upper mantle. The globally averaged profiles corresponding to these reference models contain the same first-order features: a significant increase to high attenuation at ~100 km, a sharp decrease to much weaker attenuation at ~200–250 km, and a steady

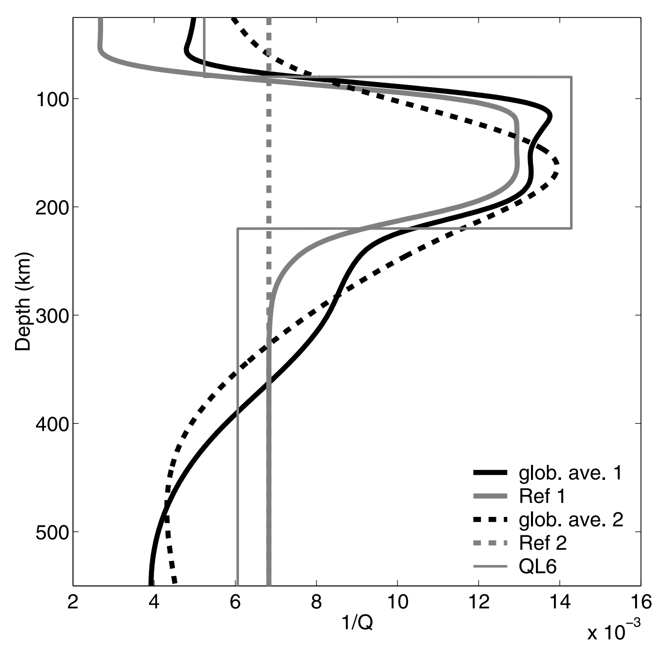

Figure 4. Globally averaged attenuation profiles for the preferred model obtained in this study. The solid black curve corresponds to the reference model indicated by the solid gray line (Ref 1). The dashed black curve corresponds to the reference model shown by the dashed gray line (Ref 2). For comparison, radial model QL6 [*Durek and Ekström*, 1996] is also shown.

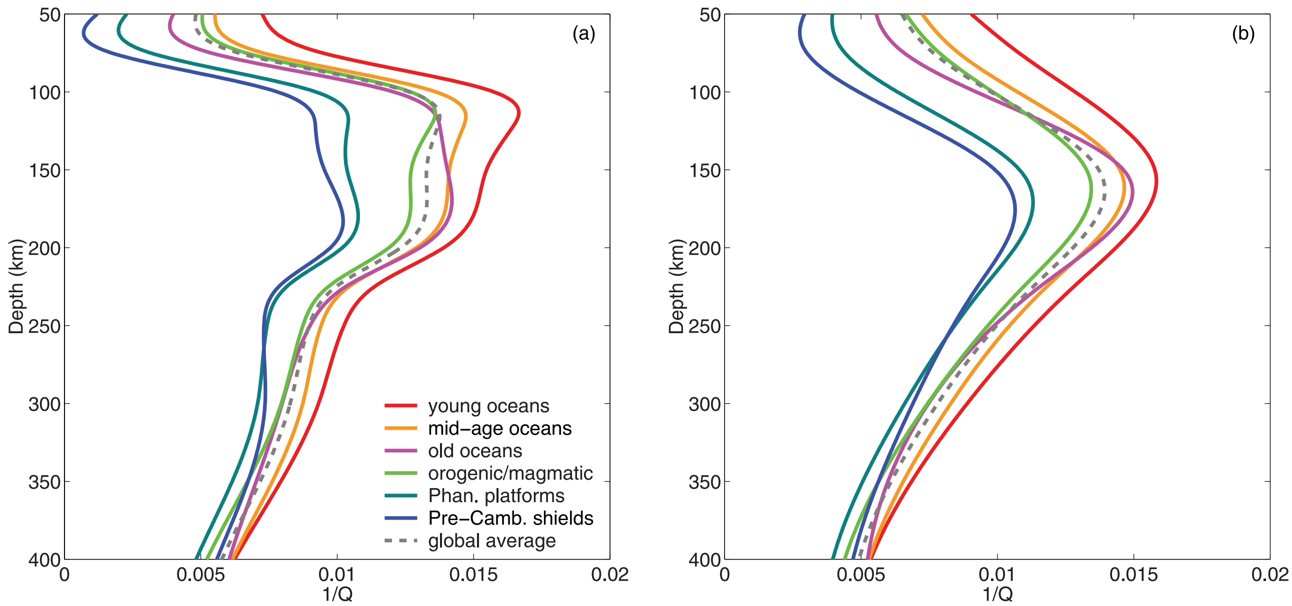

Figure 5. Regionally averaged attenuation profiles for the six tectonic regions of the GTR1 regionalization scheme. (a) Results correspond to the reference model 1 of Figure 4. (b) Results correspond to reference model 2 of Figure 4.

decrease in attenuation down to ∼450 km. Strong radial gradients in attenuation are penalized by the regularization scheme adopted here, and thus it is not possible to obtain an average global profile like that corresponding to reference model 1 in Figure 4 unless strong gradients are contained within the reference model. The fundamental mode amplitude data do not discriminate between the two average profiles in Figure 4, and the variance reduction for both cases is nearly identical.

[37] Strong regional trends in the three-dimensional attenuation model can be seen by comparing regionally averaged vertical profiles (Figure 5). The global tectonic regionalization [GTR1; *Jordan*, 1981] is used to divide the surface of the Earth into three oceanic regions, each distinguished by age of the ocean floor (0–25 Myr, 25–100 Myr, >100 Myr), and three continental regions according their tectonic behavior during the Phanerozoic (Phanerozoic orogenic zones and magmatic belts, platforms overlain by undisturbed Phanerozoic cover, and Archean and Proterozoic shields and platforms). The regional averaging is performed by populating the globe with 1442 evenly spaced points, finding the appropriate attenuation profile at each point, and determining in which region each point is located. Above 200 km, young oceanic regions are the most highly attenuating of the six areas, and in general attenuation decreases with seafloor age in Figure 5, particularly at depths shallower than 200 km. On the continents, orogenic zones and magmatic belts are characterized by stronger attenuation than the Precambrian shields and platforms and the undisturbed Phanerozoic platforms. Below ∼200–250 km, the six tectonic regions are not characterized by distinctively different attenuative properties. Comparison with the pure path estimates of oceanic and continental Rayleigh wave attenuation by *Dziewonski and Steim* [1982] shows a similar level of difference between the two regions, although the absolute Q^{-1} values of our study are slightly lower than in the earlier work.

[38] In the following sections, we discuss the results of tests performed to quantify the robustness of the model. The importance of the correction for crustal attenuation is investigated in section 4.1, the influence of regularization is explored in section 4.2, and the results of resolution tests are presented in section 4.3. Interpretation of QRFSI12 is pursued in section 5 through comparison with earlier attenuation models and with global models of shear wave velocity.

4.1. Crustal Corrections

[39] It is well established that crustal structure contributes significantly to the observed lateral variations in the phase velocity of fundamental mode surface waves, particularly for Love waves and short-period Rayleigh waves [e.g., *Ekström et al.*, 1997; *Ritsema et al.*, 2004]. Typically, in order to interpret surface-wave dispersion measurements in terms of upper-mantle velocity structure, crustal effects must be removed from the observations before inversion, and global models of crustal thickness and seismic properties, such as CRUST2.0 [*Bassin et al.*, 2000], can be used for this purpose. To date, there have been considerably fewer studies of crustal attenuation, and applicability of these studies to intermediate- and long-period Rayleigh waves is limited by assumptions about the frequency dependence of attenuation. However, attenuation in the crust is known to exist and has been explained by factors including fluid movement [*Mitchell*, 1995], crack structure [*Hauksson and Shearer*, 2006], and temperature variations, among others. Overall, Q_μ in the crust is probably fairly high [Q_μ = 300 in QL6; *Durek and Ekström*, 1996], and the sensitivity to crustal structure of the intermediate- and long-period Rayleigh waves used here is relatively small. For these reasons, it is not expected that crustal Q_μ will have an

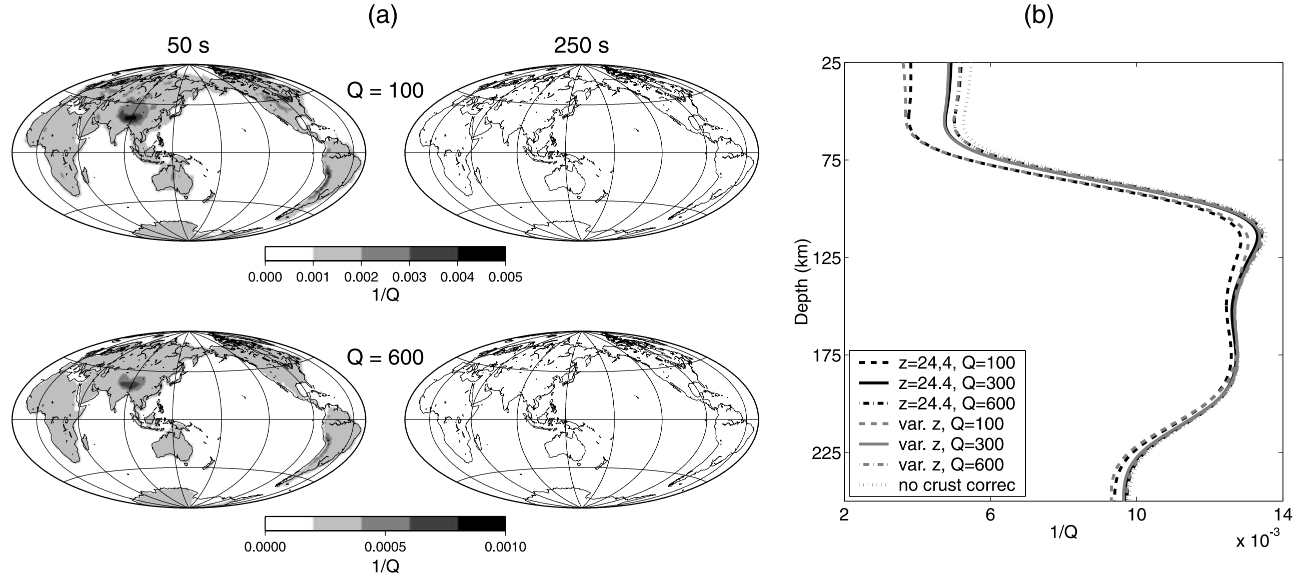

Figure 6. (a) Maps of Rayleigh wave attenuation at 50 and 250 s. For these calculations, attenuation is only nonzero in the crust. In the top panels, Q_μ in the crust is fixed at 100. In the bottom panels, Q_μ is fixed at 600. Note the different gray scales. (b) Globally averaged attenuation profiles for 7 three-dimensional attenuation models, each constructed with different assumptions about crustal attenuation, but otherwise identical. Black lines represent models for which crustal thickness is fixed at 24.4 km and Q_μ is fixed at 100, 300, and 600. Gray lines indicate models for which crustal thickness is allowed to vary laterally, and Q_μ is fixed at 100, 300, and 600. Dotted gray line shows the model for which crustal attenuation was assumed to be zero.

important effect on the upper-mantle attenuation model. However, the tests described below explore the potential influence of uncertainties in crustal attenuation on the retrieved mantle structure. Three approaches are explored: (1) Attenuation in the crust is small and can be neglected. (2) Both crustal Q_μ and crustal thickness are constant across the globe. Crustal thickness is fixed at 24.4 km [*Dziewonski and Anderson*, 1981] and crustal Q_μ values of 100, 300, and 600 are tested. (3) The crustal structure is laterally variable. In this case, the crustal thickness, seismic velocity, and density are taken from CRUST2.0 [*Bassin et al.*, 2000] and are used in the calculation of local sensitivity kernels for each $2^\circ \times 2^\circ$ grid cell. For lack of better information, Q_μ in the crust is assumed to be constant, and Q_μ values of 100, 300, and 600 are tested. For each $2^\circ \times 2^\circ$ Earth structure, surface-wave attenuation is predicted for the periods analyzed in this study, and the results are combined to yield global attenuation maps on a $2^\circ \times 2^\circ$ grid for each period (Figure 6a). Because crustal Q_μ is constant, the lateral variations in Figure 6a are due mostly to variations in crustal thickness; the largest attenuation is predicted for the regions with the thickest crust. The 250-s Rayleigh waves are fairly insensitive to attenuation in the crust. For each path in the data set, the effect of crustal attenuation on amplitude is predicted by integrating the surface-wave attenuation maps (Figure 6a) along the great circle path connecting the source and receiver. This prediction is then subtracted from each amplitude measurement prior to inversion for a mantle attenuation model as described in section 3 (i.e., equation (10)).

[40] Figure 6b shows average global shear attenuation profiles for each of the seven scenarios described above. Differences are most pronounced above 75 km. The profile with the strongest attenuation is found when crustal attenuation is assumed to be zero, since any signal of crustal attenuation contained in the amplitude data will be mapped into mantle attenuation. Conversely, the profiles with the weakest attenuation correspond to the models with crustal $Q_\mu = 100$, as this approach assumes that a larger part of the attenuation signal contained in the amplitude data occurs in the crust, and therefore less attenuation occurs in the mantle. Below 100 km, differences between the models are small.

[41] Figure 7 shows the difference maps at 50 and 100 km for two end-member cases: constant crustal thickness of 24.4 km with a high Q_μ value of 600, and variable crustal thickness with a low Q_μ value of 100. Because the variable-thickness model predicts higher attenuation in the thick continental crust (Figure 6a), attenuation in the shallow continental mantle beneath these regions must be reduced to compensate. For this reason, the assumption of a constant-thickness, high-Q_μ crust yields slightly higher mantle attenuation for the continents and lower attenuation beneath the oceans than the assumption of a variable-thickness crustal model does. At 100 km, the magnitude of the difference due to crustal effects (±0.003) is much smaller than the lateral variability in QRFSI12 (±0.013; Figure 3).

[42] In summary, our tests indicate that uncertainties in the magnitude of and lateral variability in crustal attenuation have only a small effect on the retrieved three-dimensional attenuation model. As another test to confirm that this is true, we have modified the inversion of amplitude data to solve for three additional terms that account, in an approximate way, for the influence of crustal attenuation. These terms correspond to the average crustal Q_μ in each of three

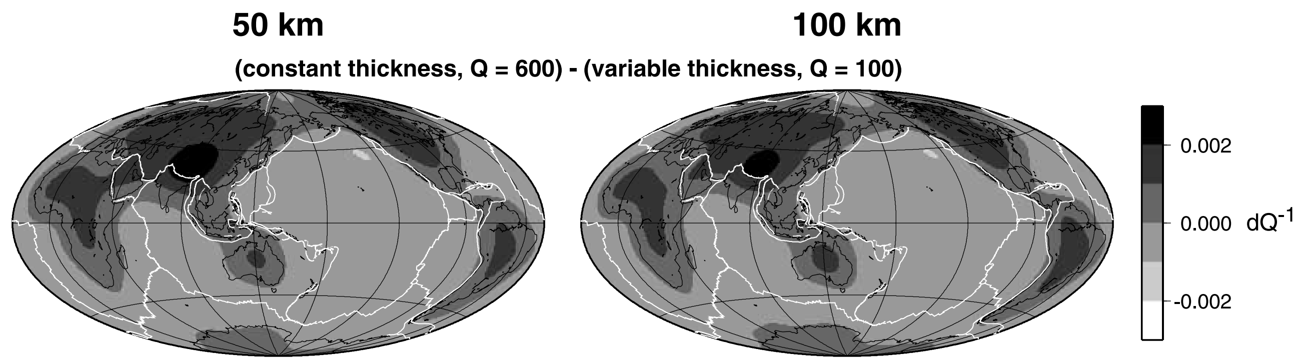

Figure 7. Difference maps, at 50 and 100 km, between two mantle attenuation models constructed with different assumptions about crustal attenuation structure. The attenuation model with variable thickness and low$-Q_\mu$ crust is subtracted from the model with constant thickness and high-Q_μ crust. Positive values indicate higher attenuation in the model for which the crust is assumed to be of constant thickness and high Q_μ. Expressed in terms of fractional perturbations to the average global value, the differences correspond to $-22-61\%$ and $-8-20\%$ at 50- and 100-km depth, respectively.

tectonic regions: all oceans, platforms and shields, and areas of active orogeny and magmatism, using the GTR1 regionalization scheme [*Jordan*, 1981]. The mantle attenuation model that results from this modified inversion is highly correlated with QRFSI12 at all depths, thus corroborating the results of our previous experiments. For our preferred model QRSFI12, crustal thickness is fixed at 24.4 km and crustal Q_μ = 600.

4.2. Influence of Regularization

[43] The solution of the inverse problem posed in equation (10) requires additional a priori information; we minimize the squared gradient of the attenuation perturbations. In this section, the influence of subjective choices about regularization on the retrieved attenuation model is explored; the effect of regularization in the vertical direction is discussed first, followed by examination of horizontal-smoothness constraints.

[44] Figure 8a shows globally averaged attenuation profiles for eight attenuation models that are derived in an identical fashion except for the weighting factor used to control vertical smoothness. Not surprisingly, assigning a larger weight to the vertical-smoothness constraint results in attenuation perturbations that are smoother as a function of

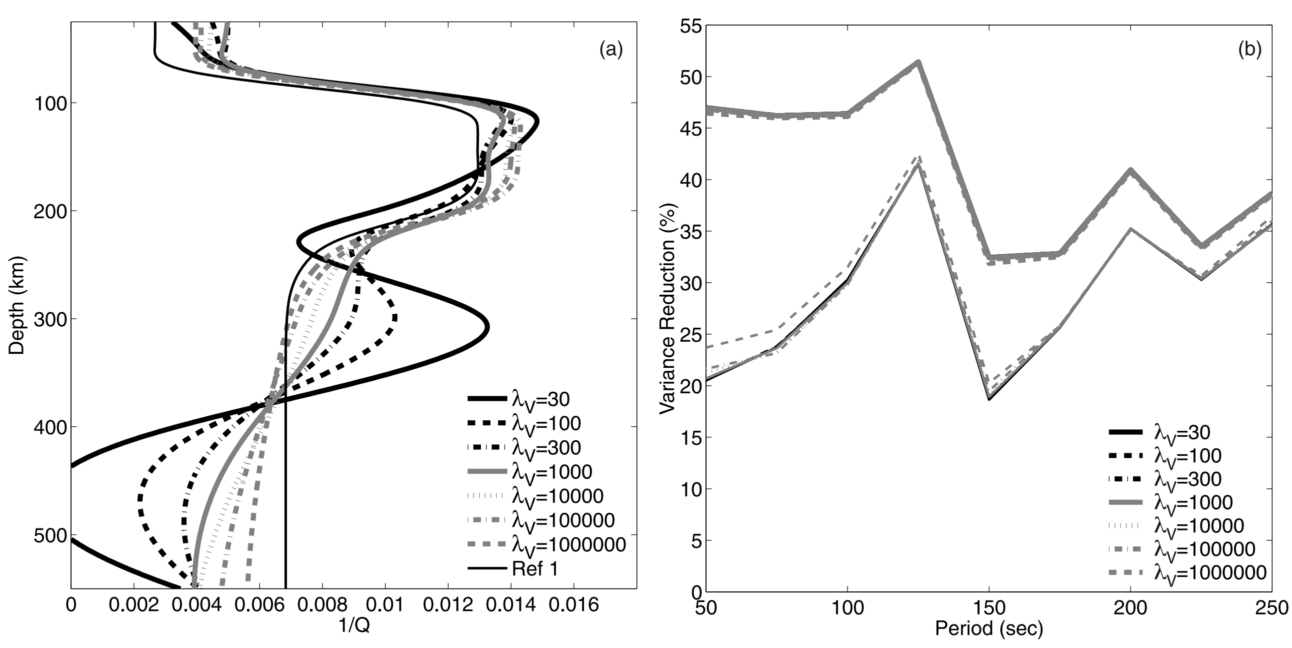

Figure 8. (a) Globally averaged attenuation profiles obtained with a range of vertical smoothness weighting factors, which control the strength of the damping. The value of the weighting factor is given in the legend; for example, λ_V = 300 is 10× stronger than λ_V = 30. The reference model 1 is also shown. (b) Effect on variance reduction of vertical smoothness weighting factor. Thin lines that plot toward the bottom of the figure indicate variance reduction calculated with only source and receiver factors; thick lines above them show the full variance reduction calculation.

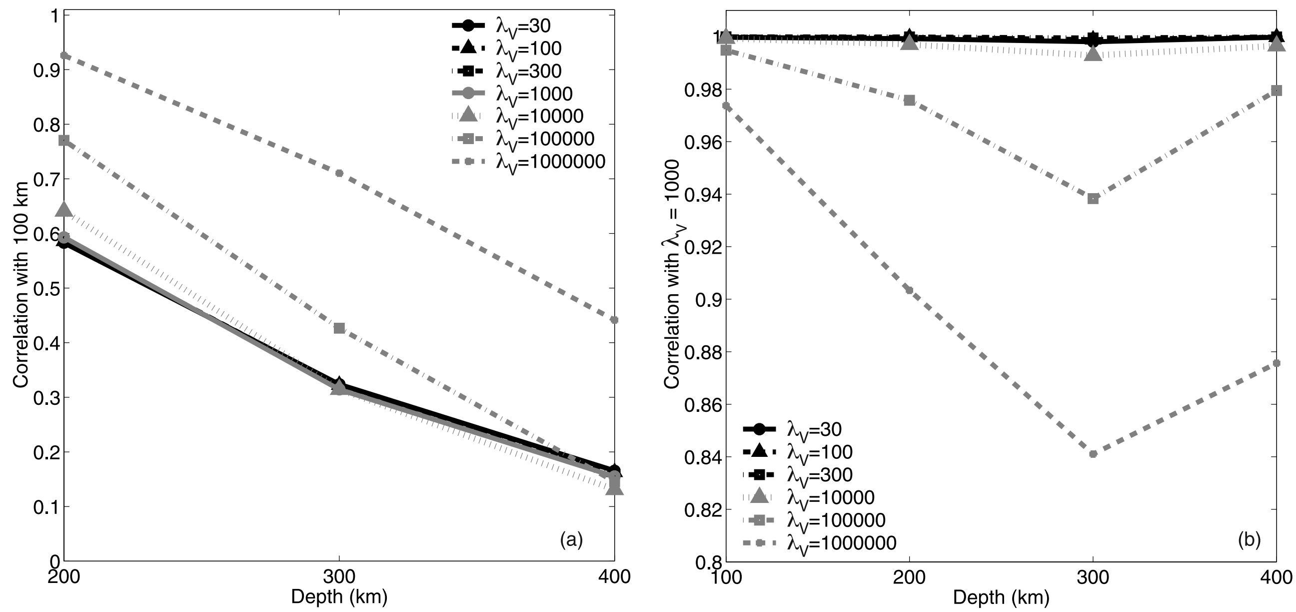

Figure 9. (a) Correlation between the attenuation model at 100 km and the attenuation model at 200 km, 300 km, and 400 km. Each line corresponds to a model constrained with a different amount of radial damping, as indicated by the legend. (b) Correlation, at four depths, between our preferred model, which corresponds to a vertical smoothness weighting factor of 1000 and models obtained with various other weighting factors.

depth and exhibit a smaller departure from the reference profile. The wild oscillatory behavior associated with the weakest constraints (i.e., $\lambda_V = 30$ and $\lambda_V = 100$ in Figure 8a) suggests that these models are not stable. Very strong constraints on smoothness (e.g., λ_V = 1,000,000) may overdamp the model and force it to align with the reference model. Overall, the effect of vertical smoothing on the variance reduction for the amplitude data sets is small; very strong damping forces some of the attenuation signal to be mapped into the source and receiver factors, as evidenced from their improved variance reduction for λ_V = 1,000,000 (Figure 8b). For our preferred model QRFSI12, a weighting factor of 1000 is chosen. The effect of radial damping does not change if a different reference model is used.

[45] For most of the radial-smoothness weighting factors tested here, the lateral patterns are not significantly affected. However, with very strong constraints on smoothness, the model is not allowed to vary much as a function of depth, and thus the horizontal structure must adjust to become more homogeneous with depth. This is apparent from an examination of the correlation coefficients between the different models at various depths in the upper mantle (Figure 9a). For example, for the majority of models investigated, structure at 100 km is correlated with structure at 200 km with a correlation coefficient of ~0.6. Weighting factors of 100,000 and 1,000,000, however, penalize differences between the model at 100 and 200 km and force the correlation up to values of 0.8–0.9. Figure 9b shows the correlation between the each of the seven models tested and the model corresponding to our preferred weighting factor of 1000; at each depth, the correlation coefficient is >0.99 except for the models obtained with weighting factors of 100,000 and 1,000,000. In summary, with the exception of the most restrictive weighting factors (here, 100,000 and 1,000,000), the subjective choice regarding how strongly the vertical-smoothness constraint should be weighted does not significantly affect data fit or the horizontal patterns of the attenuation model. However, the vertical attenuation profile varies considerably (Figure 8a), and the selection of a vertical-smoothness weighting factor is largely determined by preference for one average global profile over the others.

[46] Eight different values of the weighting factor that controls horizontal smoothness are also tested, and the effect on data variance reduction is much more significant than is the case for vertical damping (Figure 10a). At 50 s, the model obtained with a horizontal-smoothness weighting factor of 0.1 reduces variance by 6% more than does the model obtained with a weighting factor of 100. However, there is only minimal difference in data fit for weighting factors in the range 0.1–1.0. The source and receiver factors can also be influenced by the strength of the smoothness constraint, which is evident in the calculation of variance reduction using only those terms (thin lines in Figure 10a). If the attenuation model is forced to be weak (e.g., weighting factor = 100), some of the attenuation signal is mapped into the source and receiver factors. The effect is not very pronounced for values of the weighting factor between 0.1 and 1.0. As expected, the correlation between the attenuation model obtained with our preferred weighting factor of λ_H = 0.5 and models obtained with other weighting factors is highest for the weighting factors that are most similar, λ_H = 0.3 and λ_H = 1.0 (Figure 10b).

[47] In summary, the variance reduction of the amplitude data is more strongly affected by the choice of horizontal-smoothness weighting factor than by the strength of radial damping. However, models produced with horizontal weighting-factor values between λ_H = 0.3 and λ_H = 1.0 are highly correlated with each other and provide similar

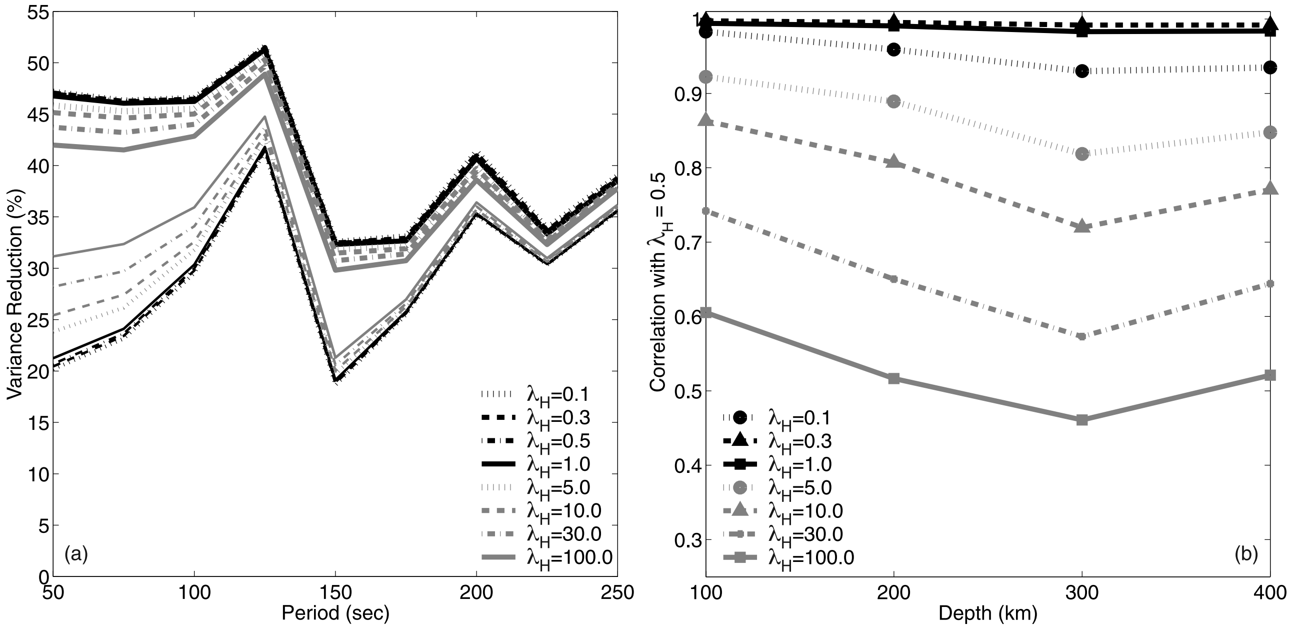

Figure 10. (a) Effect on variance reduction of choices regarding horizontal smoothness. Each line corresponds to a different amount of horizontal smoothing, as indicated by the legend. Thin lines that plot toward the bottom of the figure indicate variance reduction calculated with only source and receiver factors; thick lines above them show the full variance reduction calculation. (b) Correlation, at four depths, between our preferred model, which corresponds to a horizontal smoothness weighting factor of 0.5, and models obtained with various other weighting factors.

variance reduction. Choosing the strength of horizontal smoothing within this range is a matter of preference. For comparison to QRFSI12, λ_H = 0.3 results in peak-to-peak variations that are 110–115% of those in Figure 3, whereas λ_H = 1.0 yields variations that are 80–85% of those in QRFSI12.

4.3. Resolution Tests

[48] We have investigated the influence of regularization, uneven path coverage, and data noise on the attenuation model with several resolution tests. For the first test, the input model consists of a checkerboard pattern assigned to only the third spline (peak sensitivity at 150 km); all other splines are set equal to zero. The checkerboard pattern is set by assigning only one spherical-harmonic coefficient a nonzero value; for an input model with maximum degree L, only the spherical harmonic of degree $l = L$ and order $m = L/2$ is nonzero. A synthetic data set is generated for the path coverage of our true data set (i.e., Table 1), and these synthetic data are inverted for a three-dimensional output attenuation model using the same damping parameters that are applied to obtain QRFSI12. The results, summarized in Figures 11a and 12a, show that the input pattern is well recovered and there is little smearing in the horizontal direction. The amplitude of the recovered anomalies is spread out among the two adjacent splines, and the total recovered amplitude is weaker than the input for the shortest-wavelength structure (spherical-harmonic degree 12), as our data set contains many long paths that average the short-wavelength oscillating features in the input checkerboard. Smearing in the vertical direction is largely confined to the two adjacent splines, and the amplitude of the smeared anomalies is only a fraction of what is recovered for spline 3. With an input model dominated by spherical-harmonic degree 6, nearly 65% of the input amplitude is recovered by spline 3, and splines 2 and 4 recover the remaining 35%.

[49] When the input model is confined to deeper structure (spline 5; peak sensitivity at 300 km), the output anomalies are considerably weaker than the input, and vertical smearing is more significant (Figures 11b and 12b). However, the pattern of lateral variations is well recovered and there is little horizontal smearing. From inspection of Figure 11, it seems unlikely that structure located at 300-km depth could contaminate the attenuation model at 150 km, and vice versa. Thus the observation of two distinct patterns of attenuation in the upper mantle, above and below ~250-km depth, is robust. Furthermore, we note that the total amplitude of anomalies is not reduced significantly; it is merely spread out among spline 5 and the two adjacent splines 4 and 6 (Figure 11b).

[50] For the second test, we rotate and translate QRFSI12 to generate a synthetic attenuation model that contains the same features and spectral content as QRFSI12 but having a different orientation with respect to the distribution of paths. A synthetic data set is again generated and inverted; the results are summarized in Figure 13. The retrieved model is characterized by anomalies that are only slightly weaker than the input, and at all depths the output attenuation patterns are highly correlated with the input model. We have experimented with adding noise to the synthetic amplitude data. We estimate the characteristics of the noise at each period by analyzing the difference between amplitudes predicted by QRFSI12 and the associated source and receiver factors and the observed amplitudes (i.e., d_n^{obs} and

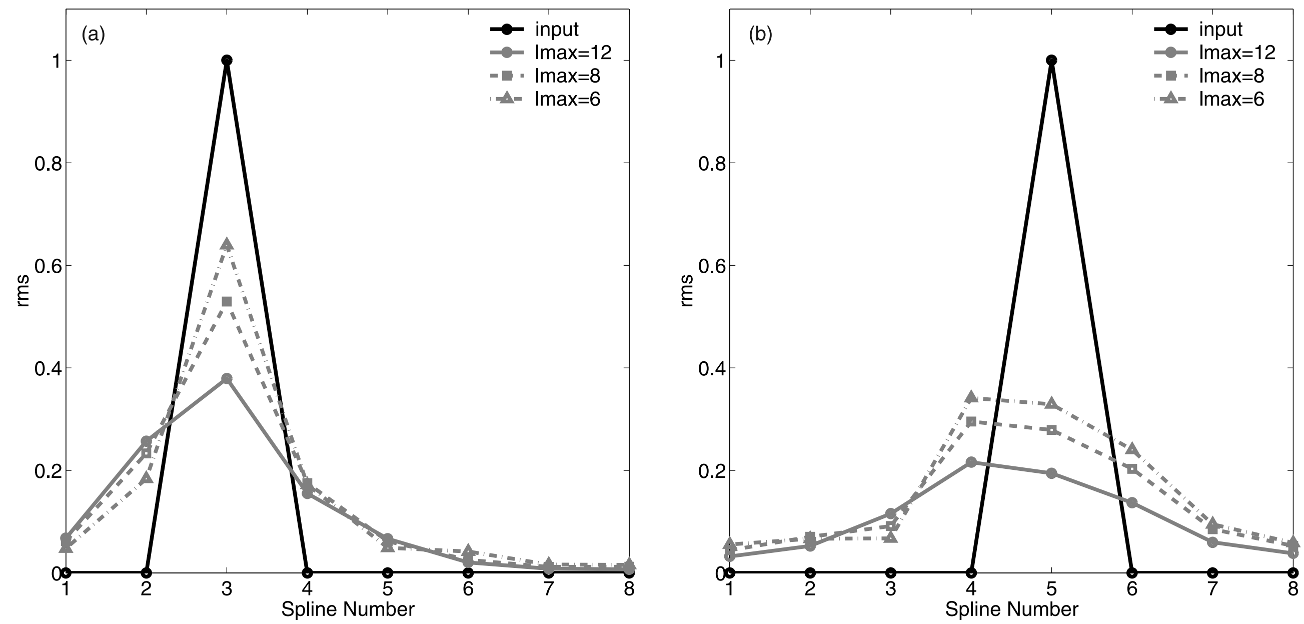

Figure 11. Summary of the checkerboard resolution tests. The root mean square (RMS) values of the input and output models are plotted as a function of spline number and are normalized by the value of the input model. Figure 2 shows the radial distribution of splines. Results corresponding to input checkerboard patterns of spherical-harmonic degrees 6, 8, and 12 are shown. (a) Checkerboard assigned only to spline 3. (b) Checkerboard assigned only to spline 5.

d_n^{pred} in equation (16)). The model obtained from inverting the synthetic data set with noise added shows slightly higher RMS than the model derived from the noise-free data set, and somewhat weaker correlation with the input model.

[51] In summary, the resolution tests indicate that little horizontal smearing is expected to result from the path coverage and regularization scheme we implement, and vertical smearing is not significant for depths shallower

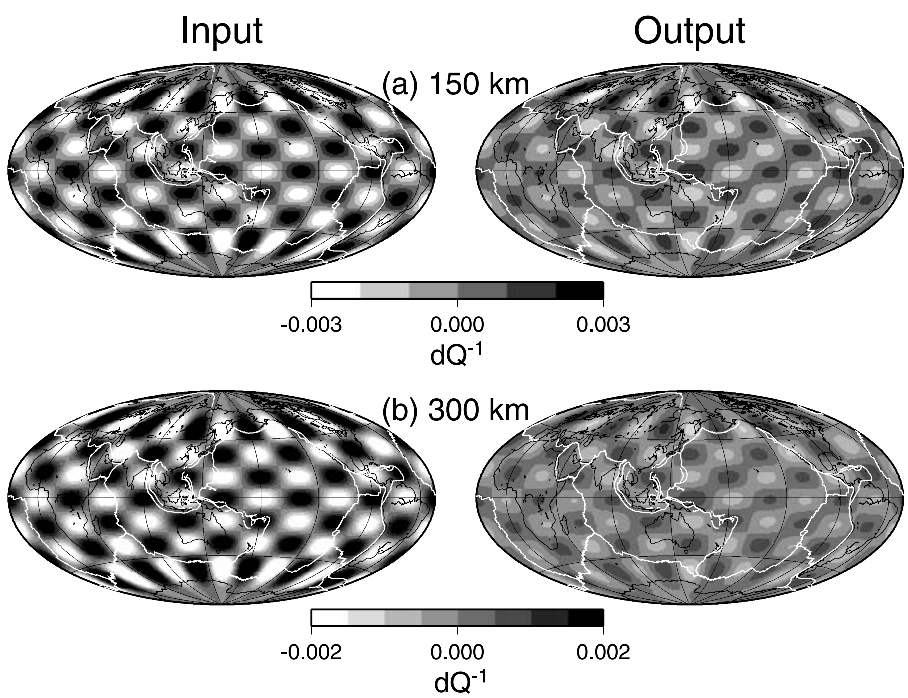

Figure 12. Input and output checkerboard patterns; only the spherical harmonic of degree 12 and order 6 is nonzero. (a) Checkerboard is assigned to spline 3 only; model shown at 150 km. (b) Checkerboard is assigned to spline 5 only; model shown at 300 km.

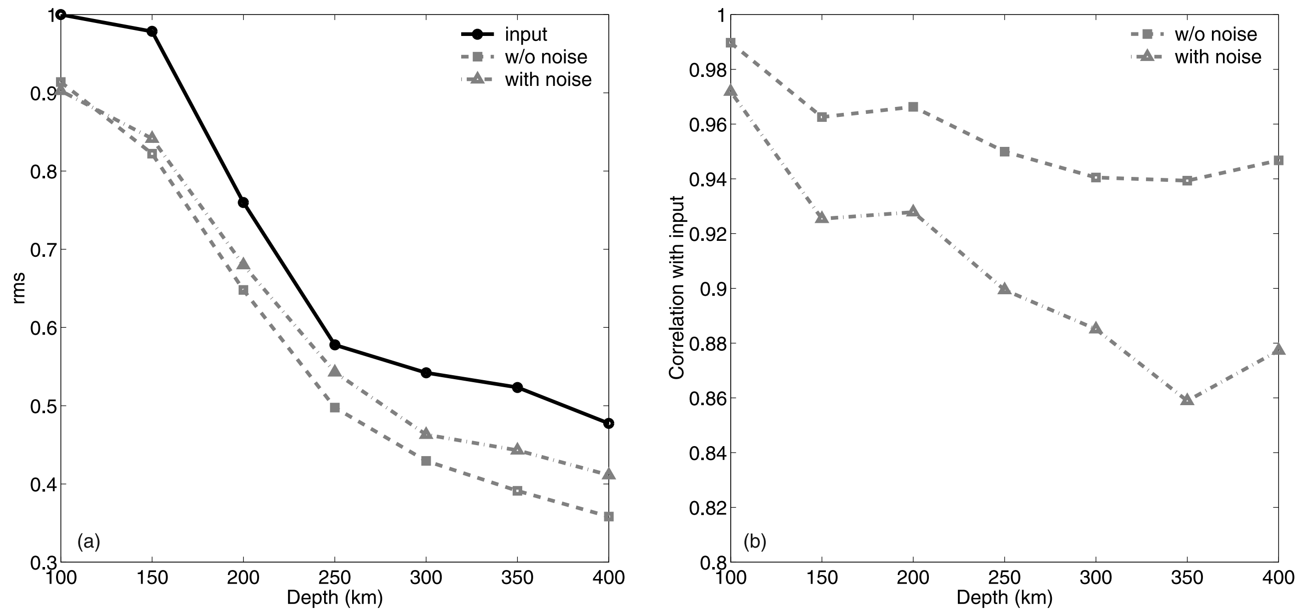

Figure 13. (a) Root mean square (RMS) value of the input and output models as a function of depth. The input model is QRFSI12 after rotation and translation. Results for output models are shown with and without noise added to the synthetic data. (b) Correlation, as a function of depth, between the input and output models.

than 250 km. The amplitude of the shortest-wavelength anomalies is likely underestimated.

5. Discussion

5.1. Comparison With Attenuation Models

[52] In this section, QRFSI12 is compared with earlier shear attenuation models. Comparison with other attenuation models helps to identify systematic similarities and differences between the models, and in particular to understand the reasons for significant discrepancies. Model QR19 [*Romanowicz*, 1995] was constructed from a limited data set of fundamental mode Rayleigh wave amplitudes in the period range 80–300 s and has a resolving wavelength equivalent to spherical-harmonic degree 6. Focusing effects were not removed from the data, although the author took

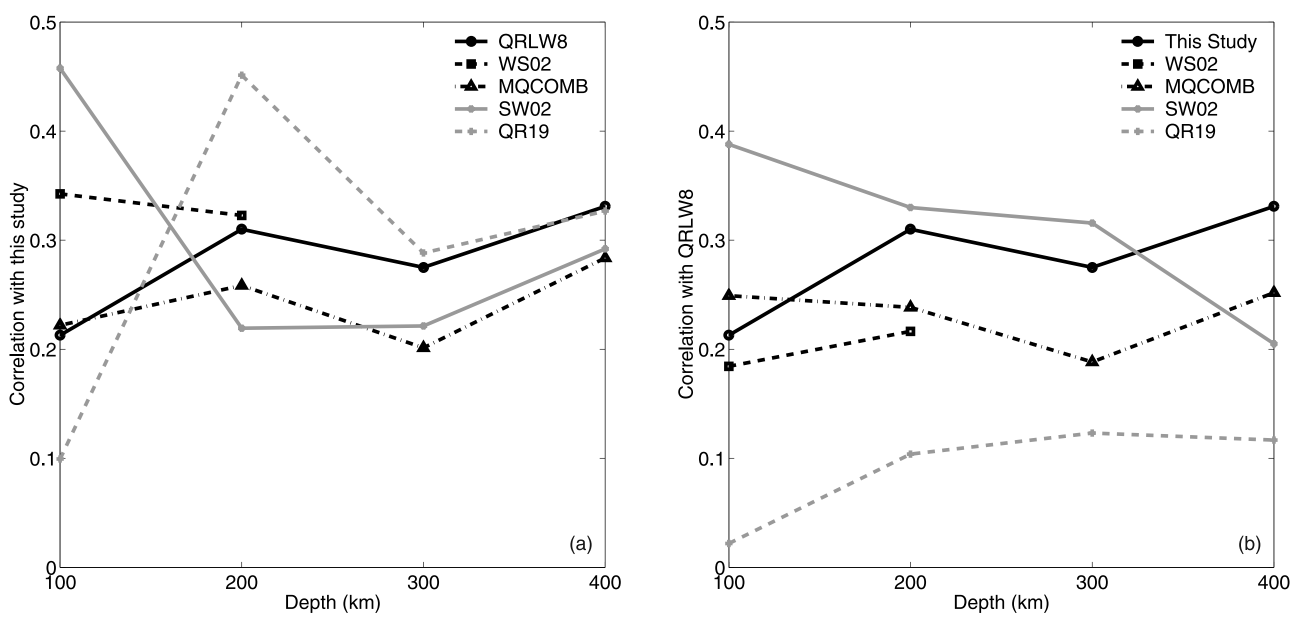

Figure 14. (a) Correlation coefficient, as a function of depth, between this study and the five other shear attenuation models examined. The correlation coefficient is calculated using spherical-harmonic degrees 1–8, and comparison with WS02 is performed only at 100-km and 200-km depth. (b) Correlation coefficient between QRLW8 [*Gung and Romanowicz*, 2004] and the five other shear attenuation models.

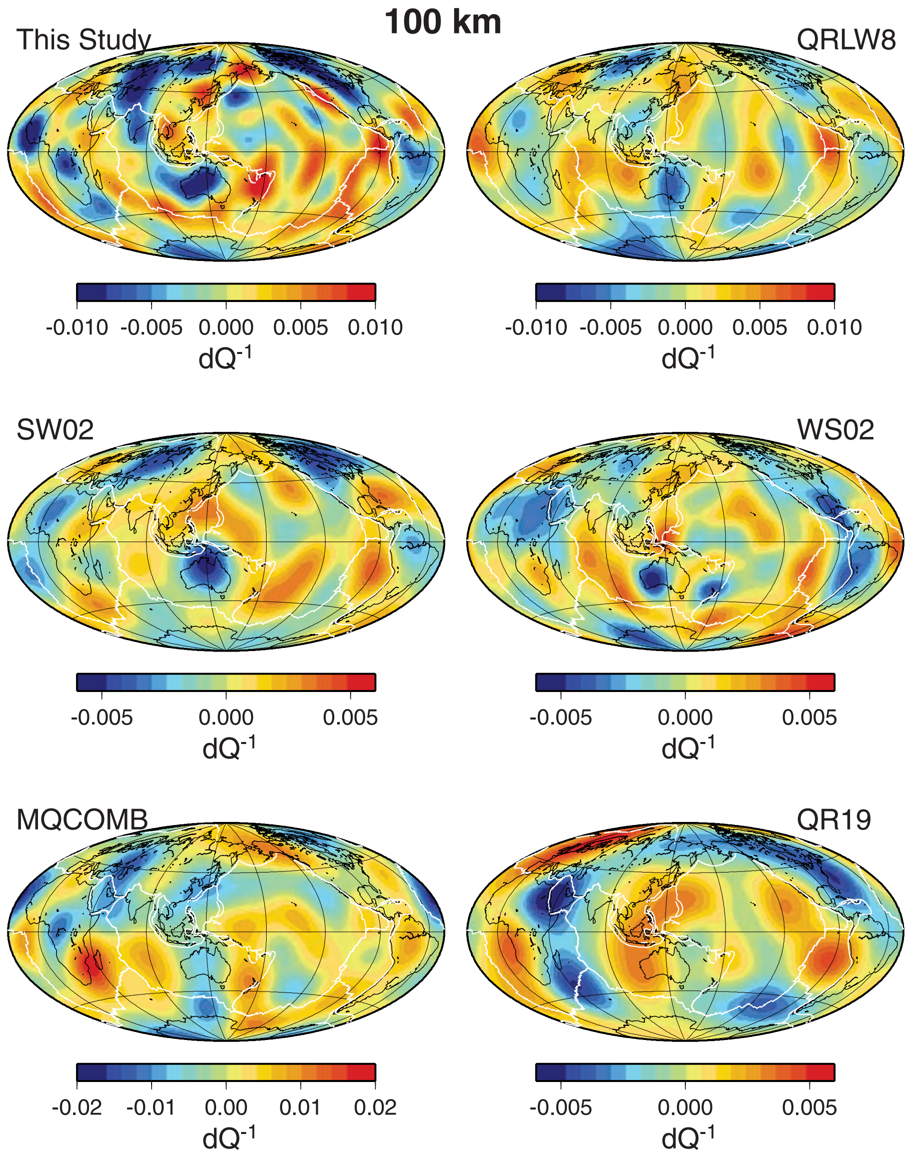

Figure 15. Comparison of QRFSI12 with five earlier attenuation models at 100 km: QRLW8 [*Gung and Romanowicz*, 2004], SW02 [*Selby and Woodhouse*, 2002], WS02 [*Warren and Shearer*, 2002], MQCOMB [*Reid et al.*, 2001], and QR19 [*Romanowicz*, 1995]. The globally averaged δQ_μ^{-1} value has been removed from each model. Note the different color scales.

care to select data that did not appear strongly contaminated by focusing effects. Model MQCOMB [*Reid et al.*, 2001] is expanded to spherical-harmonic degree 12 and was derived from ~5,000 SS-S and SSS-SS differential measurements. *Warren and Shearer* [2002] published a one-layer model of P-wave attenuation, here abbreviated WS02, that represents the top 220-km of the mantle. Their model was derived from P and PP spectra, has a nominal resolution equivalent to degree 12, and is not well resolved in parts of the southern hemisphere, in particular beneath South America and much of Africa.

[53] The attenuation model of *Selby and Woodhouse* [2002], here abbreviated SW02, was constructed from measurements of fundamental-mode Rayleigh wave amplitude in the period range 70–170 s. This degree-8 attenuation model was determined simultaneously with a period-dependent source factor for each earthquake, and focusing effects were not removed, as Selby and Woodhouse inferred from their tests that it could not be done sufficiently accurately with existing elastic-velocity models [*Selby and Woodhouse*, 2000, 2002]. Model QRLW8 [*Gung and Romanowicz*, 2004] is expanded in spherical harmonics to degree 8 and was derived from three-component surface-wave waveform data in the period range 60–400 s; in total, 31,367 waveforms were used. Focusing effects and source-amplitude uncertainty were not explicitly accounted for, although the authors performed experiments to investigate the influence of neglecting these terms.

[54] Throughout the upper mantle, these six models show only limited agreement with each other; correlation through degree 8 is <0.5 at all depths (Figure 14). In Figures 15–16, slices of the attenuation models are compared to QRFSI12

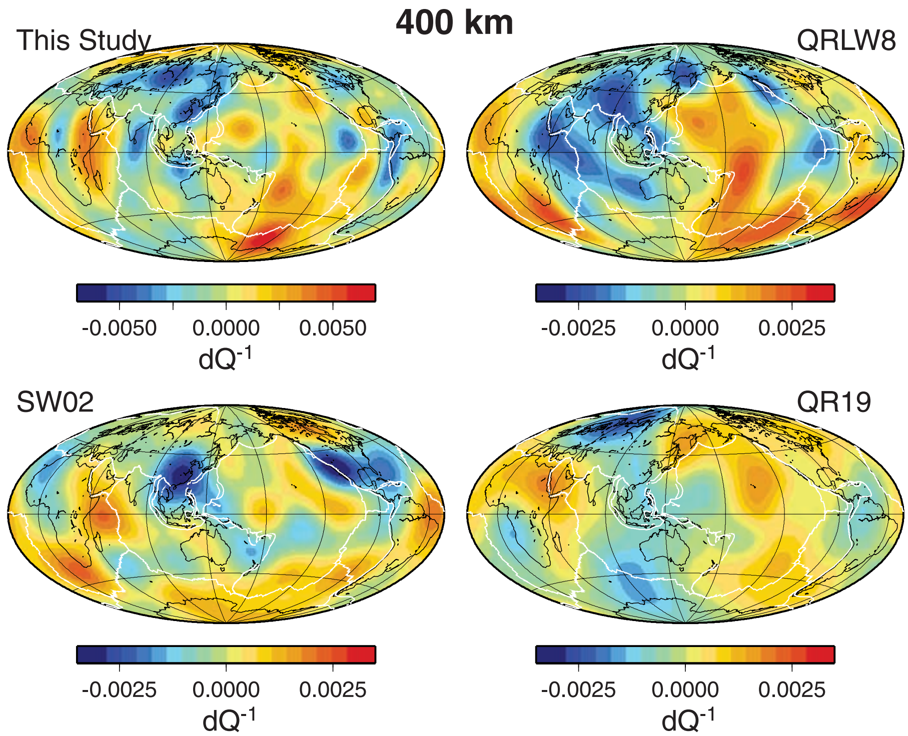

Figure 16. Comparison of attenuation models at 400 km. Note the different color scales.

at depths of 100 and 400 km. The amplitude of the lateral Q_{μ}^{-1} variations differs considerably between the models, and thus different color scales are used so that the patterns contained within the models can be compared. At 100 km, all of the models exhibit low attenuation in the vicinity of some stable continental interiors. For example, western Africa is a low-attenuation feature in all models except QR19, and at least parts of the Canadian Shield are characterized by high Q_{μ} in all models. However, MQCOMB and QR19 exhibit only average attenuation for western Australia and eastern South America. It is intriguing that QRFSI12, MQCOMB, and WS02 all contain a linear zone of high attenuation extending southeast of Hawaii.

[55] The most significant differences at 100 km between this study and the other attenuation models can be seen along mid-ocean ridges, which are consistently high-attenuation features in QRFSI12. Models WS02 and MQCOMB contain higher-than-average attenuation in the vicinity of the East Pacific Rise, the Pacific–Antarctic ridge, and the ridge system in the Indian Ocean, and QRLW8 exhibits high attenuation along the southwest- and mid-Indian ridges and the northernmost East Pacific Rise. However, the southern East Pacific Rise and Pacific–Antarctic ridge are characterized by lower-than-average attenuation in QRLW8, QR19, and SW02. This observation is difficult to explain in terms of temperature variations, given that material beneath the ridge axis at this depth is expected to be of higher temperature than older oceanic lithosphere located some distance from the rise. Because ridges are slow-velocity zones at 100 km (e.g., Figure 18), they can cause the focusing of wave energy and an associated amplitude increase. These anomalously large amplitudes will map into anomalously low attenuation if focusing effects are not accounted for (cf. Figures 11 and 12 in DE06a), and we believe this can explain the discrepancies along some mid-ocean ridges and along western North America.

[56] At depths of 300 and 400 km, QRLW8 and QR19 exhibit better agreement with this study than does SW02 (Figure 14), perhaps because only periods <170 s were used in the construction of that model, limiting its depth resolution. QRFSI12 and QRLW8 show reasonably good agreement in the Pacific, including a bifurcated high-attenuation anomaly in the southern Pacific and generally low attenuation beneath the subduction zones in the western Pacific (Figure 16). However, beneath eastern Africa, QRFSI12 agrees better with SW02 and QR19, which are all characterized by high attenuation in this area.

5.2. Comparison With Velocity Models

[57] For the purpose of interpreting QRFSI12, comparison with velocity models is the most powerful approach, since attenuation and velocity have different sensitivity to factors such as temperature, composition, and the presence of melt or fluids. In general, correlation between QRFSI12 and the global velocity models is much stronger than the correlation between QRFSI12 and global attenuation models; this is apparent from a comparison of Figures 14a and 17a . QRFSI12 is also better correlated with shear velocity models throughout the upper mantle than any of the other global attenuation models examined here (Figure 17b). Joint interpretation of these two data sets is explored more thoroughly in a separate paper (C. A. Dalton et al., Seismological and experimental observations of shear velocity and attenuation: A global comparison, submitted to *Earth and Planetary Science Letters*, 2008); in this section, images of the attenuation and velocity models are presented and discussed.

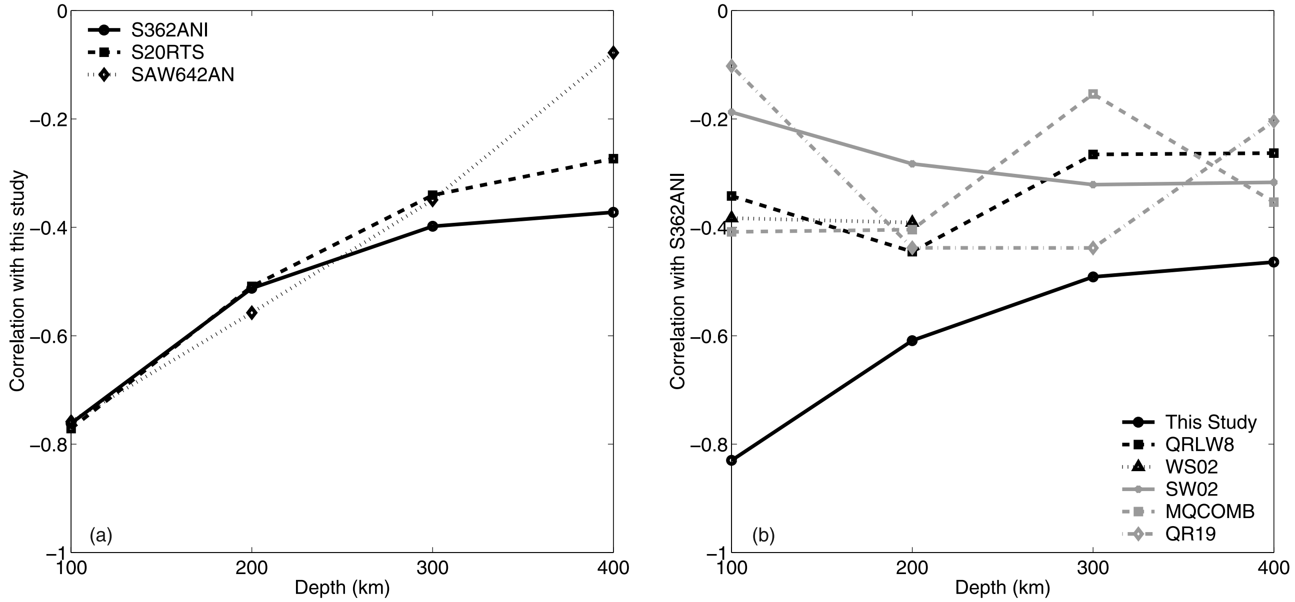

Figure 17. (a) Correlation coefficient, as a function of depth, between this study and three shear velocity models. The correlation coefficient is calculated using spherical-harmonic degrees 1–12. (b) Correlation, as a function of depth, between velocity model S362ANI and six shear attenuation models. Correlation coefficient is calculated using degrees 1–8.

[58] S362ANI [*Kustowski et al.*, 2008] and SAW642AN [*Panning and Romanowicz*, 2006] are global three-dimensional models of radially anisotropic shear wave velocity throughout the mantle. S362ANI was constructed from large data sets of surface-wave phase anomalies, long-period waveforms, and body wave traveltimes, and it has a resolving wavelength equivalent to spherical-harmonic degree 18. SAW642AN was derived from three-component surface-wave and body wave waveforms and has a resolving wavelength equivalent to spherical-harmonic degree 24. S20RTS [*Ritsema et al.*, 1999] contains three-dimensional isotropic shear wave velocity variations expanded in spherical harmonics to degree 20 and was built from data sets of Rayleigh wave phase anomalies, body wave traveltimes, and observations of normal-mode splitting. In the uppermost mantle, velocity anomalies in S20RTS are appropriate for vertically polarized shear waves, since only Rayleigh waves were used; Voigt average velocities are plotted for S362ANI and SAW642AN, i.e., $\frac{\delta V_S}{V_S} = \frac{1}{3}\frac{\delta V_{SH}}{V_{SH}} + \frac{2}{3}\frac{\delta V_{SV}}{V_{SV}}$.

[59] At 100 km, the attenuation model QRFSI12 is strongly anticorrelated with the velocity models, with correlation coefficients ranging between −0.75 and −0.78 (Figure 17a). Mid-ocean ridges are characterized by slow velocity and high attenuation (Figure 18). The Lau Basin behind the Tonga subduction zone is also a high-attenuation and slow-velocity feature, as is westernmost North America. Many Precambrian cratons are characterized by low attenuation and fast velocity at this depth. This is true of the Canadian Shield of North America, the west African, Kalahari, Congo, and Tanzanian cratons of Africa, much of Siberia, western Australia, and the South American craton. In the Pacific, the attenuation model has in common with S20RTS a high-attenuation/slow-velocity region extending from the central Pacific toward Hawaii. This feature is not very strong in the anisotropic-velocity models S362ANI and SAW642AN. The presence of this feature in our attenuation model, which is derived exclusively from V_{SV}-sensitive Rayleigh waves, may suggest the existence of radially anisotropic attenuation, a subject that is of great geophysical interest but is beyond the scope of this study. The most significant difference between the attenuation and velocity models can be seen beneath the Bering Sea and Aleutian islands, where a zone of high attenuation has no obvious counterpart in the velocity models.

[60] At 200 km, the conclusions are largely the same, although the correlation is not as high, ranging between −0.55 and −0.6. At 300 and 400 km, the velocity models are less similar to each other, and thus their correlation with the attenuation model is more variable (Figure 17). However, there are several large-scale features that all four models have in common, including a broad zone of high attenuation and low velocity located just east of the Pacific–Antarctic–Australia triple junction, generally low attenuation and fast velocity along many of the subduction zones in the western Pacific, and high attenuation and low velocity under eastern Africa (Figure 19). There are notable differences as well. For example, at 400 km, India is a low-attenuation feature with average or slightly slow velocities, and the Philippine Sea and South China Basin are characterized by fast velocity and generally average attenuation.

[61] Cross-sections through QRFSI12 and velocity models S362ANI and S20RTS are shown in Figures 20–21. In Figure 20, fast velocities and low attenuation extend to depths of 150–200 km beneath the Kalahari craton and parts of the Zambia and Tanzania cratons to the southwest. Toward the northeastern portion of the cross section, there is an abrupt transition to slow velocities and high attenuation beneath Ethiopia, the Red Sea, and the Gulf of Aden. The attenuation model shows a secondary peak in attenuation in the depth range 200–300 km that has no obvious counter-

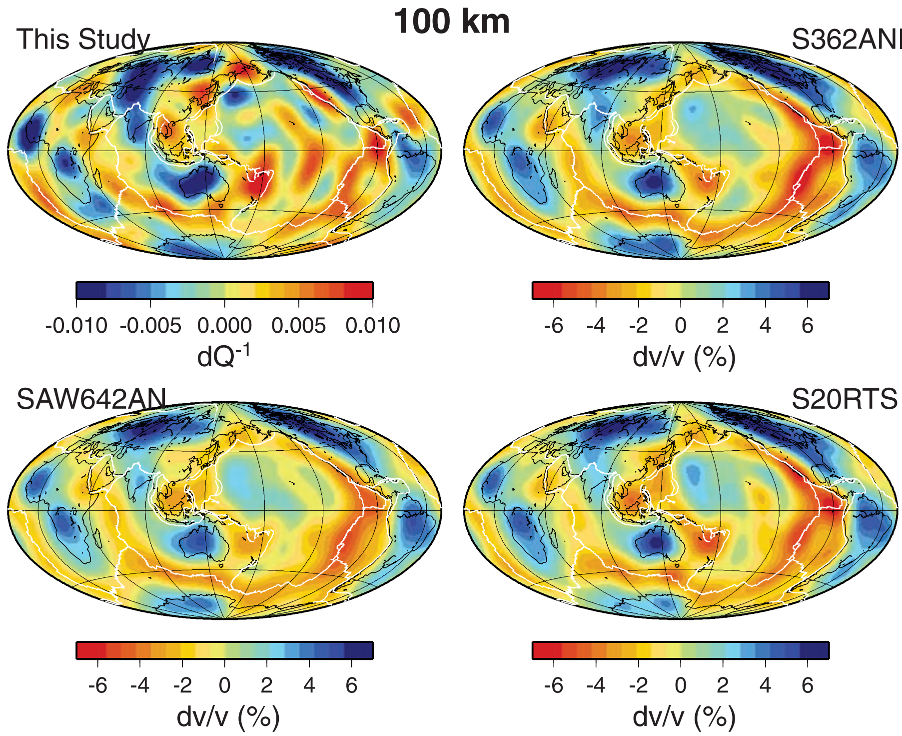

Figure 18. Comparison of QRFSI12 with three models of shear wave velocity at 100 km. Each map is expanded in spherical harmonics to degree 12, and the globally averaged value has been removed.

part in the two global velocity models but is consistent with regional tomographic studies that show a broad and deep-seated low-wave speed anomaly [*Benoit et al.*, 2006].

[62] Beneath North America (Figure 21), the cross-sections show clearly the division of the continent into a high-attenuation, slow-velocity, tectonically active western region and a low-attenuation, fast-velocity tectonically stable eastern region. The slow velocities and high attenuation to the west terminate at depths of ~200 km. The fast velocities beneath the North American craton extend to depths

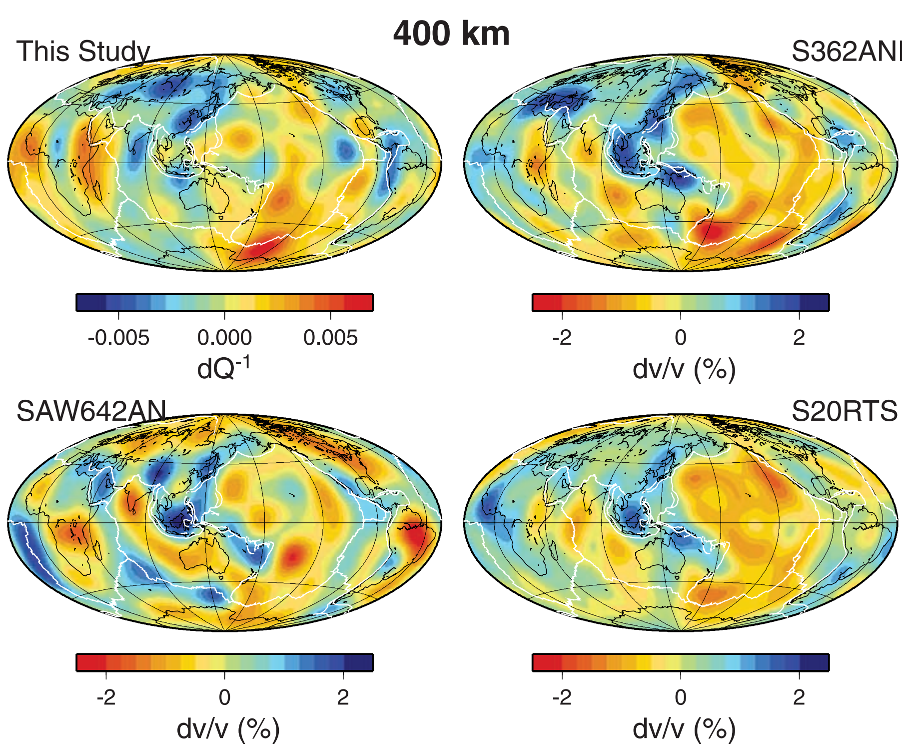

Figure 19. As in Figure 18 but at 400 km.

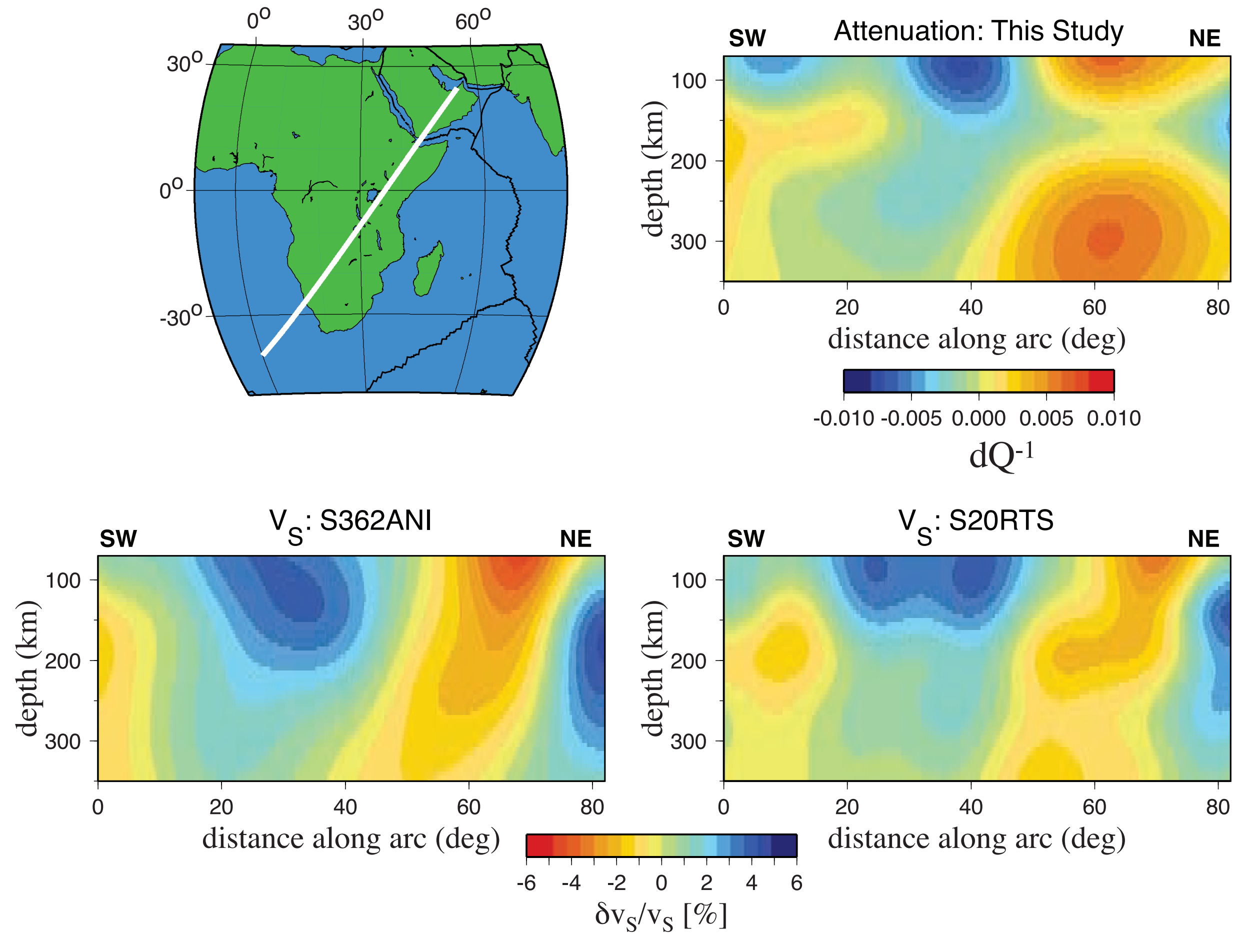

Figure 20. Cross-section through QRFSI12 and two shear velocity models. The cross-section extends laterally through southern, central, and eastern Africa and in depth from 70–350 km. The white line in the map (top left) indicates the region shown in cross-section.

>200 km; however, the low-attenuation signal associated with the craton appears to terminate at 150 km. It is important to remember that the attenuation model likely has larger uncertainties than the velocity models do, and interpreting the finer-scale details of the attenuation model should be done with caution. However, the difference in the depth extent of the velocity and attenuation anomalies associated with the craton provides an example of the potential value of having two independent data sets to interpret. If attenuation is considered to be a proxy for temperature, as is often assumed [e.g., *Jackson et al.*, 2002], then the anomalously fast velocities observed below 150 km require a nonthermal origin. Compositional heterogeneity, in particular iron depletion due to extraction of basaltic melt, is one plausible explanation [e.g., *Lee*, 2003].

5.3. Similarity of Velocity and Attenuation Models

[63] Considering the high level of agreement between the three-dimensional attenuation model described here and three-dimensional models of shear wave velocity, it is worthwhile to investigate how well the features in the velocity models can explain the Rayleigh wave amplitude data set. In other words, how well does an attenuation model that is merely a velocity model scaled by a constant factor fit the data? Such an undertaking is also motivated by an underlying physical relationship between attenuation and velocity; an increase in temperature causes an increase in attenuation and a decrease in wave speed [e.g., *Faul and Jackson*, 2005]. If temperature is the primary factor controlling both quantities, then a strong anticorrelation between attenuation and velocity is expected. In this section, the ability of a scaled velocity model to explain a data set of surface-wave amplitudes is explored. We also examine the effectiveness of damping the attenuation perturbations toward a three-dimensional reference model that is a scaled velocity model. For both sets of tests, we hope to understand, through examination of data fit, to what extent the patterns in global velocity models agree with lateral attenuation variations.

[64] To set up the inverse problem, we assume a three-dimensional shear wave velocity model in which variations in velocity, $\frac{\delta v}{v}(r,\theta,\phi)$, are expanded with spherical harmonics in the horizontal direction and cubic B-splines in the radial direction,

$$\frac{\delta v}{v}(r,\theta,\phi) = \sum_{k=1}^{K}\sum_{l=0}^{L}\sum_{m=-l}^{l} V_{klm} B_k(r) Y_{lm}(\theta,\phi). \qquad (19)$$

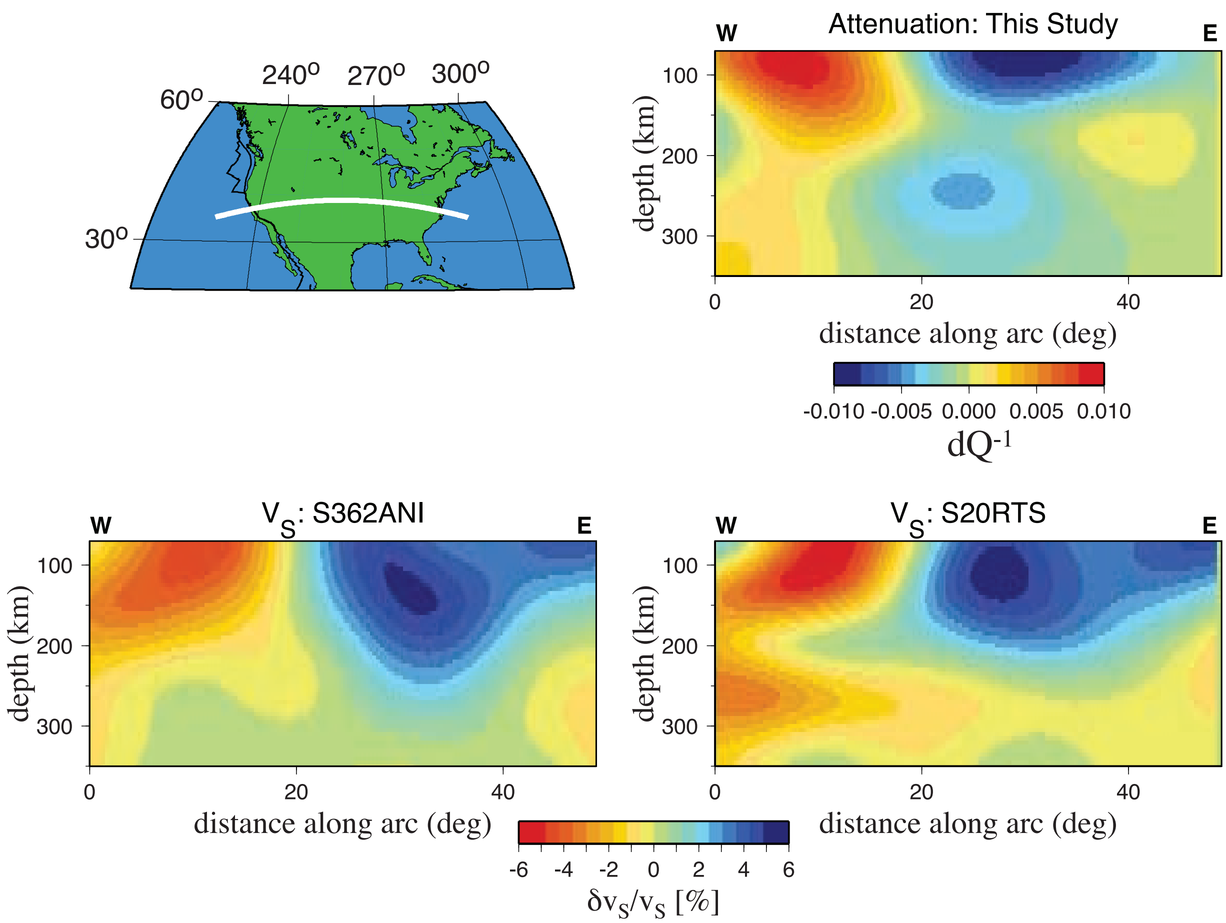

Figure 21. As in Figure 20 but across North America.

[65] We desire that the deviation in attenuation away from a reference value be linearly related to the velocity perturbation, such that

$$\delta Q_{\mu}^{-1}(r,\theta,\phi) = c(r)\cdot\frac{\delta v}{v}(r,\theta,\phi) = \sum_{k=1}^{K} D_k B_k(r) + \sum_{k=1}^{K} c_k \sum_{l=0}^{L} \sum_{m=-l}^{l} V_{klm} B_k(r) Y_{lm}(\theta,\phi), \tag{20}$$

where $c(r)$ is the scaling factor, which may or may not depend on depth, and the coefficients D_k describe the average global deviation of attenuation away from the reference value. In this expression, attenuation variations are forced to be proportional to velocity variations. Thus the amplitude data corrected for focusing effects, A_{ij}^{CF}, are used to solve for the unknown coefficients D_k and c_k as well as frequency-dependent source and receiver factors A_i^{S} and A_j^{I}, and equation (10) becomes

$$\begin{aligned}\frac{-2U}{\omega X_{ij}}\ln A_{ij}^{\mathrm{CF}} + Q_{PREM}^{-1} - \frac{1}{X_{ij}}\int_{S_i}^{R_j}\int_{r_c}^{a}\mu_0(r)K_{\mu}(\omega,r)Q_{\mu}^{-1}(r,\theta,\phi)r^2 drds \\ - \frac{1}{X_{ij}}\int_{S_i}^{R_j}\int_{0}^{r_c}\mu_0(r)K_{\mu}(\omega,r)Q_{\mathrm{ref}}^{-1}(r)\cdot r^2 drds \\ = \frac{-2U}{\omega X_{ij}}\left[\ln A_i^S + \ln A_j^I\right] + \sum_k D_k Z_k(\omega) \\ + \sum_k c_k \sum_l \sum_m V_{klm}\overline{Y_{lm}} Z_k(\omega).\end{aligned} \tag{21}$$

[66] The coefficients V_{klm} describe the velocity model to be scaled and are known; in practice, the model S362ANI [*Kustowski et al.*, 2008], expanded in spherical harmonics to degree 12, is used as the input velocity model. Although a least squares solution to equation (21) can be found without regularization, it is necessary to apply a radial-smoothness constraint to the coefficients D_k in order to obtain a non-oscillatory and nonnegative attenuation profile. The effect of damping the average global profile is very similar to the examples shown in Figure 8a, and as discussed in section 4.2, the variance reduction is not strongly affected by constraints on the D_k coefficients. We first performed an inversion to determine a velocity scaling factor that does not vary with depth; this depth-independent factor is not affected by the amount of damping applied to the D_k values. The best-fitting value of c, -0.12, predicts attenuation perturbations that are much weaker at 300 and 400 km than is found by direct comparison of models QRFSI12 and S362ANI (Figure 22a).

[67] In order to solve for a scaling factor that varies with depth, we apply a roughness minimization constraint to the c_k coefficients (Figure 22a). The overall trend of the scaling factors with depth is not affected by the strength of damping: in general, a larger (more negative) scaling factor is required in the depth range 200–400 km than for depths above 200 km, in agreement with the results obtained from comparison of QRFSI12 and S362ANI. The average scaling factor over the depth range 50–500 km is close to the

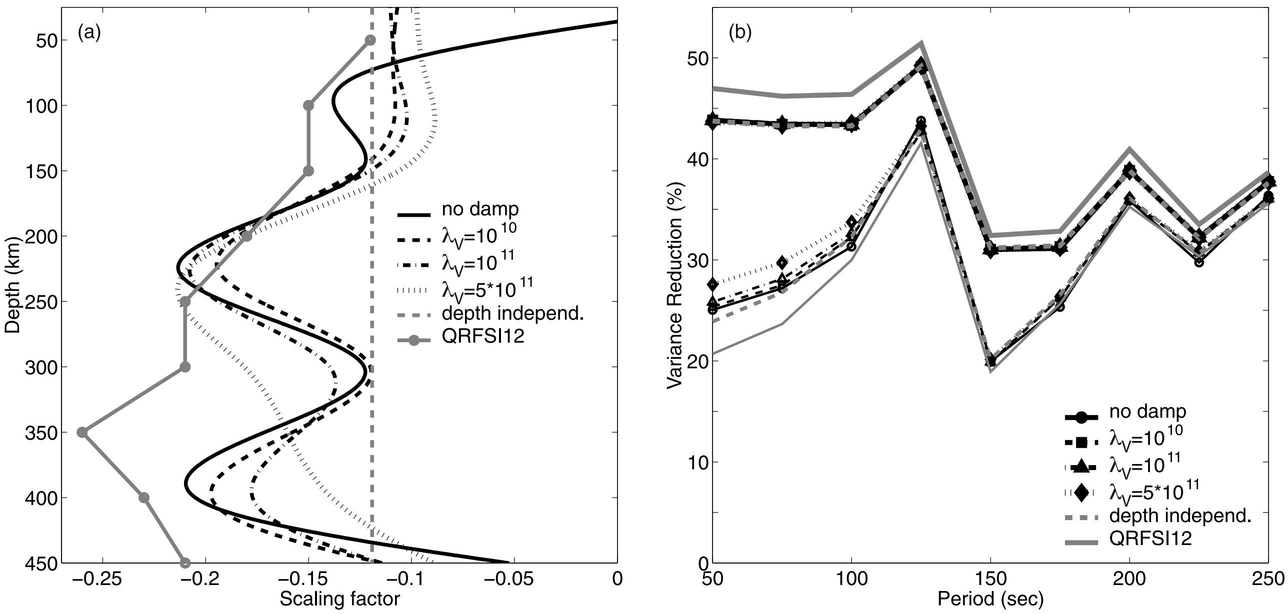

Figure 22. (a) Comparison of the depth-dependent scaling factor, shown for a range of damping parameters λ_V, with the depth-independent scaling factor. Also shown is the best-fitting scaling factor between QRFSI12 and S362ANI. (b) Variance reduction for the attenuation model obtained with a depth-dependent velocity-scaling factor; results are shown for a range of weighting factors λ_V that control the radial smoothness of the scaling factor. Thin lines that plot toward the bottom of the figure indicate variance reduction calculated with only source and receiver factors; thick lines above them show the full variance reduction calculation. For comparison, values are also shown for QRFSI12, as well as for the case of a depth-independent scaling factor.

depth-independent value of −0.12. Applying a vertical-smoothness constraint to the scaling factor results in profiles that are less oscillatory with depth, particularly in the depth range 200–400 km, and also pushes the scaling factor in the shallow part of the model toward less negative values. The full variance reduction, calculated using the three-dimensional attenuation model plus source and receiver factors, is not very sensitive to how much the scaling factor is damped (Figure 22b). However, the variance reduction calculated for the source and receiver factors alone is more significantly affected, as the source and receiver terms absorb some of the attenuation structure for the more highly damped cases.

[68] In the construction of global seismological models, the choice of reference model can be very important, as this is the model toward which the inversion is damped. We have explored the range of attenuation models retrieved when the reference model contains three-dimensional variations in attenuation; as before, the sensitivity kernels are calculated in PREM. Predictions of the three-dimensional reference model are subtracted from the data vector, and we invert for perturbations with respect to this model. Equation (10) is therefore modified to allow a three-dimensional reference model, $Q^{-1}_{\mathrm{ref}}(r,\theta,\phi)$. The solution depends considerably on the strength of damping; stronger damping results in a model more similar to the three-dimensional reference model. We investigate trade-offs between data fit and the degree of similarity to the reference model.

[69] In practice, we choose as the reference model the model that results from scaling S362ANI by the depth-independent factor of −0.12. With only weak damping applied to the inversion, the resulting attenuation model is nearly identical to our preferred attenuation model QRFSI12 (Figure 23). With increased constraints on horizontal roughness, the attenuation model becomes less similar to the preferred model and exhibits better agreement with the starting model, a scaled version of S362ANI. The value of the horizontal-smoothness weighting factor at which the correlation with the starting model and with QRFSI12 is roughly equal occurs for λ_H = 10 at 100 km and λ_H = 5 at 400 km. The variance reduction provided by these two "compromise" models is worse than QRFSI12 by 1–2% at all periods. If we suspected that our amplitude data set was not of sufficient quality to alone constrain attenuation structure, and if we assumed that attenuation and velocity should be well correlated with one another, then these particular models would represent a reasonable compromise between these two pieces of information. However, because factors other than temperature influence velocity and attenuation, and because the relationship between velocity and attenuation depends on temperature, pressure, frequency, and grain size [*Faul and Jackson*, 2005], we prefer not to make these simplifying assumptions.

[70] The results of this section suggest that while there is quite good agreement between QRFSI12 and global models of shear wave velocity, particularly at shallow depths, the Rayleigh wave amplitude data insist on attenuation variations that are not identical to velocity variations. The origin of these differences may be a physical mechanism, such as laterally variable rock composition, grain size, water content, or partial-melt content. Alternatively, the differences may reflect data uncertainty, approximate theory, and im-

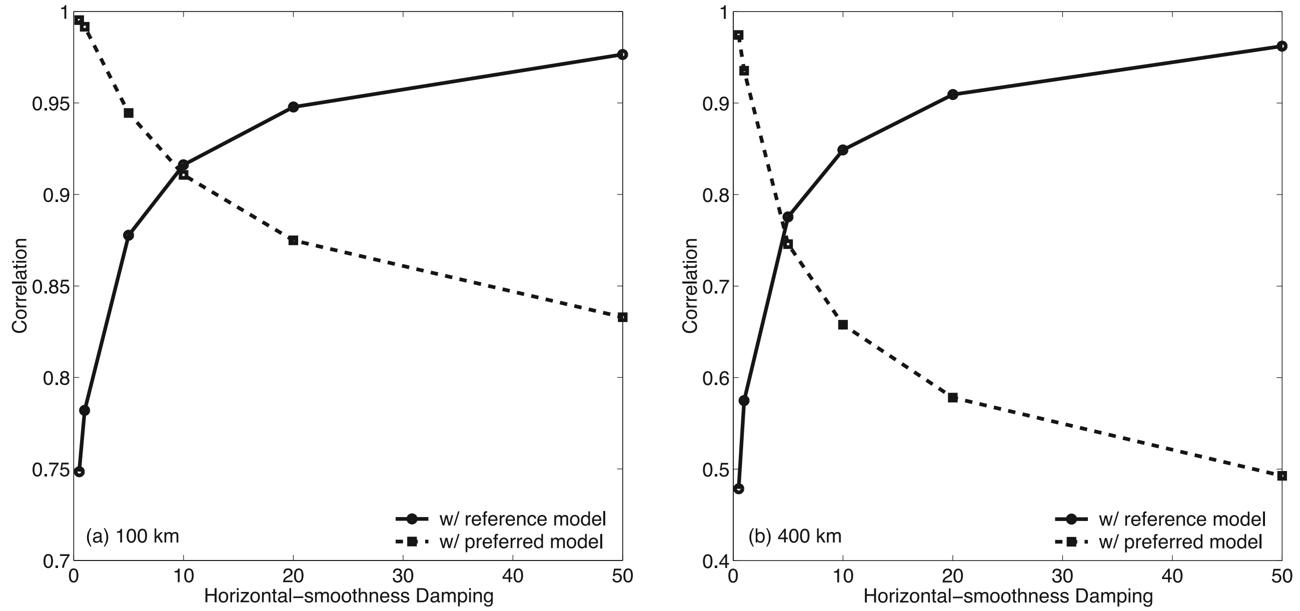

Figure 23. (a) Trade-offs between the correlation with the reference model (a scaled version of S362ANI) and our preferred model (QRFSI12) as a function of the strength of horizontal smoothing. Calculated at 100 km. (b) As on left, but at 400 km.

perfect resolution of velocity and attenuation models. Ultimately, a joint inversion of traveltime and amplitude data may help to clarify the source of these differences.

6. Conclusions

[71] We have presented a new three-dimensional global model of shear attenuation in the upper mantle. A large data set of Rayleigh wave amplitudes is inverted for the coefficients of the model and frequency-dependent source and receiver factors. Focusing effects are removed from the data prior to inversion. QRFSI12 contains large lateral variations in attenuation at all depths, and strong penalties against horizontal roughness result in significant increases in data misfit. At shallow depths, QRFSI12 shows a strong correlation with plate tectonic features, and different tectonic provinces are clearly characterized by distinct attenuative properties. At depths >250 km, the model is dominated by high attenuation in the southeastern Pacific and eastern Africa.

[72] Agreement between QRFSI12 and earlier attenuation models is generally much weaker than the level of agreement between many of the global shear velocity models [e.g., *Panning and Romanowicz*, 2006]. Agreement between QRFSI12 and velocity models is strong, particularly at depths <300 km, which suggests that the same factors that control velocity also control attenuation. We have performed experiments to investigate whether the amplitude data set can be fit as well by the patterns in global velocity models as by QRFSI12. The results indicate that this is not the case, and that subtle regional differences between the two quantities may be robust. In *Dalton* [2007] and a forthcoming paper, we further investigate the level of agreement between velocity and attenuation by incorporating laboratory constraints on the temperature, frequency, and grain-size dependence of attenuation and velocity [*Jackson et al.*, 2002; *Faul and Jackson*, 2005].

[73] **Acknowledgments.** This material is based on work supported by a National Science Foundation Graduate Research Fellowship and NSF grants EAR-02-07608 and EAR-06-09111. All figures were made with GMT [*Wessel and Smith*, 1991; http://gmt.soest.hawaii.edu].

References

Anderson, D. L. (1967), The anelasticity of the mantle, *Geophys. J. R. Astron. Soc.*, *14*, 135–164.

Anderson, D. L., and J. W. Given (1982), Absorption band *Q* model for the Earth, *J. Geophys. Res.*, *87*, 3893–3904.

Backus, G. E., and J. F. Gilbert (1967), Numerical applications of a formalism for geophysical inverse problems, *Geophys. J. R. Astron. Soc.*, *13*, 247–276.

Bassin, C., G. Laske, and G. Masters (2000), The current limits of resolution for surface wave tomography in North America, *Geophys. J. R. Astron. Soc.*, *81*, Fall Meet Suppl., F897.

Benoit, M. H., A. A. Nyblade, and J. C. VanDecar (2006), Upper mantle P wave speed variations beneath Ethiopia and the origin of the Afar Hot spot, *Geology*, *34*, 329–332.

Bhattacharyya, J., G. Masters, and P. Shearer (1996), Global lateral variations of shear wave attenuation in the upper mantle, *J. Geophys. Res.*, *101*, 22,273–22,289.

Canas, J. A., and B. J. Mitchell (1978), Lateral variation of surface-wave anelastic attenuation across Pacific, *Bull. Seismol. Soc. Am.*, *68*, 1637–1650.

Canas, J. A., and B. J. Mitchell (1981), Rayleigh wave attenuation and its variation across the Atlantic Ocean, *Geophys. J. R. Astron. Soc.*, *67*, 159–176.

Chan, W. W., and Z. A. Der (1988), Attenuation of multiple ScS in various parts of the world, *Geophys. J. Int.*, *92*, 303–314.

Dahlen, F. A., and J. Tromp (1998), *Theoretical Global Seismology*, p. 1025, Princeton Univ. Press, Princeton, N. J.

Dalton, C. A. (2007), The global attenuation structure of the upper mantle, Ph.D. thesis, Harvard Univ.

Dalton, C. A., and G. Ekström (2006a), Global models of surface-wave attenuation, *J. Geophys. Res.*, *111*, B05317, doi:10.1029/2005JB003997.

Dalton, C. A., and G. Ekström (2006b), Constraints on global maps of phase velocity from surface-wave amplitudes, *Geophys. J. Int.*, *167*, doi:10.1111/j.1365-246X.2006.03142.x.

Durek, J. J., and G. Ekström (1996), A radial model of anelasticity consistent with long-period surface-wave attenuation, *Bull. Seismol. Soc. Am.*, *86*, 144–158.

Dziewonski, A. M., and D. L. Anderson (1981), Preliminary reference Earth model, *Phys. Earth Planet. Inter.*, *25*, 297–356.
Dziewonski, A. M., and J. M. Steim (1982), Dispersion and attenuation of mantle waves through waveform inversion, *Geophys. J. R. Astron. Soc.*, *70*, 503–527.
Dziewonski, A. M., T.-A. Chou, and J. H. Woodhouse (1981), Determination of earthquake source parameters from waveform data for studies of global and regional seismicity, *J. Geophys. Res.*, *86*, 2825–2852.
Ekström, G., J. Tromp, and E. W. F. Larson (1997), Measurements and global models of surface wave propagation, *J. Geophys. Res.*, *102*, 8137–8157.
Ekström, G., C. A. Dalton, and M. Nettles (2006), Observations of time-dependent errors in the long-period instrument gain at global seismic stations, *Seismol. Res. Lett.*, *77*, 12–22.
Faul, U. H., and I. Jackson (2005), The seismological signature of temperature and grain size variations in the upper mantle, *Earth Planet. Sci. Lett.*, *234*, 119–134.
Flanagan, M. P., and D. A. Wiens (1990), Attenuation structure beneath the Lau back arc spreading center from teleseismic *S* phases, *Geophys. Res. Lett.*, *17*, 2117–2120.
Gung, Y., and B. Romanowicz (2004), Q tomography of the upper mantle using three-component long-period waveforms, *Geophys. J. Int.*, *157*, 813–830.
Hammond, W. C., and E. D. Humphreys (2000a), Upper mantle seismic wave velocity: Effects of realistic partial melt geometries, *J. Geophys. Res.*, *105*, 10,975–10,986.
Hammond, W. C., and E. D. Humphreys (2000b), Upper mantle seismic wave attenuation: Effects of realistic partial melt distribution, *J. Geophys. Res.*, *105*, 10,987–10,999.
Hauksson, E., and P. M. Shearer (2006), Attenuation models (Q_P and Q_S) in three dimensions of the southern California crust: Inferred fluid saturation at seismogenic depths, *J. Geophys. Res.*, *111*, B05302, doi:10.1029/2005JB003947.
Jackson, I., J. D. Fitz Gerald, U. H. Faul, and B. H. Tan (2002), Grain-size-sensitive seismic wave attenuation in polycrystalline olivine, *J. Geophys. Res.*, *107*(B12), 2360, doi:10.1029/2001JB001225.
Jackson, I., U. H. Faul, J. D. Fitz Gerald, and B. H. Tan (2004), Shear wave attenuation and dispersion in melt-bearing olivine polycrystals: 1. Specimen fabrication and mechanical testing, *J. Geophys. Res.*, *109*, B06201, doi:10.1029/2003JB002406.
Jordan, T. H. (1981), Global tectonic regionalization for seismological data analysis, *Bull. Seismol. Soc. Am.*, *71*, 1131–1141.
Kanamori, H., and D. L. Anderson (1977), Importance of physical dispersion in surface wave and free oscillation problems: Review, *Rev. Geophys. Space Phys.*, *15*, 105–112.
Karato, S. (1993), Importance of anelasticity in the interpretation of seismic tomography, *Geophys. Res. Lett.*, *20*, 1623–1626.
Karato, S. (2003), Mapping water content in the upper mantle, in *Inside the Subduction Factory*, *Geophys. Monogr. Ser.*, vol. 138, pp. 135–152, AGU, Washington, D. C.
Kustowski, B., G. Ekström, and A. M. Dziewoński (2008), The anisotropic shear-wave velocity structure of the Earth's mantle: A global model, *J. Geophys. Res.*, *113*, B06306, doi:10.1029/2007JB005169.
Laske, G., and G. Masters (1996), Constraints on global phase velocity maps from long-period polarization data, *J. Geophys. Res.*, *101*, 16,059–16,075.
Lawrence, J. F., and M. Wysession (2006), Seismic evidence for subduction-transported water in the lower mantle, in *Earth's Deep-Water Cycle*, *Geophys. Monogr. Ser.*, vol. 168, pp. 251–261, AGU, Washington, D. C.
Lawrence, J. F., P. M. Shearer, and G. Masters (2006), Mapping attenuation beneath North America using waveform cross-correlation and cluster analysis, *Geophys. Res. Lett.*, *33*, L07315, doi:10.1029/2006GL025813.
Lay, T., and T. C. Wallace (1988), Multiple *ScS* attenuation and travel-times beneath western North America, *Bull. Seismol. Soc. Am.*, *78*, 2041–2061.
Lee, C.-T. A. (2003), Compositional variation of density and seismic velocities in natural peridotites at STP conditions: Implications for seismic imaging of compositional heterogeneities in the upper mantle, *J. Geophys. Res.*, *108*(B9), 2441, doi:10.1029/2003JB002413.
Liu, H. P., D. L. Anderson, and H. Kanamori (1976), Velocity dispersion due to anelasticity; implications for seismology and mantle composition, *Geophys. J. R. Astron. Soc.*, *47*, 41–58.
Mitchell, B. J. (1995), Anelastic structure and evolution of the continental crust and upper mantle from seismic surface wave attenuation, *Rev. Geophys.*, *33*, 441–462.
Molnar, P., and J. Oliver (1969), Lateral variations of attenuation in the upper mantle and discontinuities in the lithosphere, *J. Geophys. Res.*, *74*, 2648–2682.
Panning, M. P., and B. Romanowicz (2006), A three-dimensional radially anisotropic model of shear velocity in the whole mantle, *Geophys. J. Int.*, *167*, doi:10.1111/j.1365-246X.2006.03100.x.
Reid, F. J. L., J. H. Woodhouse, and H. J. van Heijst (2001), Upper mantle attenuation and velocity structure from measurements of differential S phases, *Geophys. J. Int.*, *145*, 615–630.
Resovsky, J., J. Trampert, and R. D. van der Hilst (2005), Error bars for the global seismic *Q* profile, *Earth Planet. Sci. Lett.*, *230*, 413–423.
Revenaugh, J., and T. H. Jordan (1991), Mantle layering from *ScS* reverberations: 3. The upper mantle, *J. Geophys. Res.*, *96*, 19,781–19,810.
Ritsema, J., H.-J. van Heijst, and J. H. Woodhouse (1999), Complex shear wave velocity structure imaged beneath Africa and Iceland, *Science*, *286*, 1925–1928.
Ritsema, J., L. A. Rivera, D. Komatitsch, J. Tromp, and H.-J. van Heijst (2002), Effects of crust and mantle heterogeneity on *PP/P* and *SS/S* amplitude ratios, *Geophys. Res. Lett.*, *29*(10), 1430, doi:10.1029/2001GL013831.
Ritsema, J., H.-J. van Heijst, and J. H. Woodhouse (2004), Global transition zone tomography, *J. Geophys. Res.*, *109*, B02302, doi:10.1029/2003JB002610.
Romanowicz, B. (1990), The upper mantle degree 2: Constraints and inferences from global mantle wave attenuation measurements, *J. Geophys. Res.*, *95*, 11,051–11,071.
Romanowicz, B. (1995), A global tomographic model of shear attenuation in the upper mantle, *J. Geophys. Res.*, *100*, 12,375–12,394.
Roth, E. G., D. A. Wiens, L. M. Dorman, J. Hildebrand, and S. C. Webb (1999), Seismic attenuation tomography of the Tonga-Fiji region using phase pair methods, *J. Geophys. Res.*, *104*, 4795–4809.
Roth, E. G., D. A. Wiens, and D. P. Zhao (2000), An empirical relationship between seismic attenuation and velocity anomalies in the upper mantle, *Geophys. Res. Lett.*, *27*, 601–604.
Sailor, R. V., and A. M. Dziewonski (1978), Measurement and interpretation of normal mode attenuation, *Geophys. J. R. Astron. Soc.*, *53*, 559–581.
Selby, N. D., and J. H. Woodhouse (2000), Controls on Rayleigh wave amplitudes: Attenuation and focusing, *Geophys. J. Int.*, *142*, 933–940.
Selby, N. D., and J. H. Woodhouse (2002), The Q structure of the upper mantle: Constraints from Rayleigh wave amplitudes, *J. Geophys. Res.*, *107*(B5), 2097, doi:10.1029/2001JB000257.
Sheehan, A. F., and S. C. Solomon (1992), Differential shear-wave attenuation and its lateral variation in the North-Atlantic region, *J. Geophys. Res.*, *97*, 15,339–15,350.
Sipkin, S. A., and T. H. Jordan (1979), Frequency dependence of Q_{ScS}, *Bull. Seismol. Soc. Am.*, *69*, 1055–1079.
Sipkin, S. A., and T. H. Jordan (1980), Regional variation of Q_{ScS}, *Bull. Seismol. Soc. Am.*, *70*, 1071–1102.
Sipkin, S. A., and J. Revenaugh (1994), Regional variation of attenuation and travel-time in China from analysis of multiple-*ScS* phases, *J. Geophys. Res.*, *99*, 2687–2699.
Stachnik, J. C., G. A. Abers, and D. H. Christensen (2004), Seismic attenuation and mantle wedge temperatures in the Alaska subduction zone, *J. Geophys. Res.*, *109*, B10304, doi:10.1029/2004JB003018.
Trampert, J., and J. H. Woodhouse (1995), Global phase velocity maps of Love and Rayleigh waves between 40 and 150 seconds, *Geophys. J. Int.*, *122*, 675–690.
van der Hilst, R. D., S. Widyantoro, and E. R. Engdahl (1997), Evidence for deep mantle circulation from global tomography, *Nature*, *386*, 578–584.
Venkataraman, A., A. A. Nyblade, and J. Ritsema (2004), Upper mantle *Q* and thermal structure beneath Tanzania, East Africa from teleseismic *P* wave spectra, *Geophys. Res. Lett.*, *31*, L15611, doi:10.1029/2004GL020351.
Warren, L. M., and P. M. Shearer (2002), Mapping lateral variations in upper mantle attenuation by stacking *P* and *PP* spectra, *J. Geophys. Res.*, *107*(B12), 2342, doi:10.1029/2001JB001195.
Wessel, P., and W. H. F. Smith (1991), Free software helps map and display data, *Eos Trans. AGU*, *72*, 441.
Woodhouse, J. H., and A. M. Dziewonski (1984), Mapping the upper mantle: Three-dimensional modeling of Earth structure by inversion of seismic waveforms, *Geophys. J. R. Astron. Soc.*, *89*, 5953–5986.
Woodhouse, J. H., and Y. K. Wong (1986), Amplitude, phase and path anomalies of mantle waves, *Geophys. J. R. Astron. Soc.*, *87*, 753–773.
Woodward, R. L., and G. Masters (1991), Global upper mantle structure from long-period differential travel times, *J. Geophys. Res.*, *96*, 6351–6377.
Yang, Y., D. W. Forsyth, and D. S. Weeraratne (2007), Seismic attenuation near the East Pacific Rise and the origin of the low-velocity zone, *Earth Planet. Sci. Lett.*, *258*, 260–268.

C. A. Dalton and A. M. Dziewoński, Department of Earth and Planetary Sciences, Harvard University, 20 Oxford Street, Cambridge, MA 02138, USA. (dalton@ldeo.columbia.edu)
G. Ekström, Lamont-Doherty Earth Observatory of Columbia University, 61 Route 9W, Palisades, NY 10964, USA. (ekstrom@ldeo.columbia.edu)